



1 **A comparative assessment of the uncertainties of global surface-ocean CO₂ estimates using a
2 machine learning ensemble (CSIR-ML6 version 2019a) – have we hit the wall?**

3 Luke Gregor^{1,2}, Alice D. Lebehot^{1,2}, Schalk Kok³, Pedro M. Scheel Monteiro¹

4 ¹SOCCO, Council for Scientific and Industrial Research, Cape Town, 7700, South Africa

5 ²MaRe, Marine Research Institute, University of Cape Town, Cape Town, 7700, South Africa

6 ³Department of Mechanical & Aeronautical Engineering, University of Pretoria, Pretoria, 0028, South Africa

7 Correspondence to: Luke Gregor (lukegre@gmail.com)

8 **Abstract.** Over the last decade, advanced statistical inference and machine learning have been
9 used to fill the gaps in sparse surface ocean CO₂ measurements (Rödenbeck et al. 2015). The
10 estimates from these methods have been used to constrain seasonal, interannual and decadal
11 variability in sea-air CO₂ fluxes and the drivers of these changes (Landschützer et al. 2015, 2016,
12 Gregor et al. 2018). However, it is also becoming clear that these methods are converging towards
13 a common bias and RMSE boundary: *the wall*, which suggests that pCO₂ estimates are now
14 limited by both data gaps and scale-sensitive observations. Here, we analyse this problem by
15 introducing a new gap-filling method, an ensemble of six machine learning models (CSIR-ML6
16 version 2019a), where each model is constructed with a two-step clustering-regression approach.
17 The ensemble is then statistically compared to well-established methods. The ensemble,
18 CSIR-ML6, has an RMSE of 17.16 µatm and bias of 0.89 µatm when compared to a test-dataset
19 kept separate from training procedures. However, when validating our estimates with independent
20 datasets, we find that our method improves only incrementally on other gap-filling methods. We
21 investigate the differences between the methods to understand the extent of the limitations of
22 gap-filling estimates of pCO₂. We show that disagreement between methods in the South Atlantic,
23 southeastern Pacific and parts of the Southern Ocean are too large to interpret the interannual
24 variability with confidence. We conclude that improvements in surface ocean pCO₂ estimates will
25 likely be incremental with the optimisation of gap-filling methods by (1) the inclusion of
26 additional clustering and regression variables (e.g. eddy kinetic energy), (2) increasing the
27 sampling resolution. Larger improvements will only be realised with an increase in CO₂
28 observational coverage, particularly in today's poorly sampled areas.



29

1 Introduction

30 The ocean plays a crucial role in mitigating against climate change by taking up about a third of the
31 anthropogenic carbon dioxide (CO_2) emissions (Sabine et al. 2004; Khatiwala et al., 2013; McKinley et al.
32 2016). While the mean state in the global contemporary marine CO_2 uptake is a widely-used benchmark (Le
33 Quéré et al., 2018), underlying assumptions and limited confidence regarding the variability and long-term
34 evolution of this sink persist. Sparse observations of surface ocean CO_2 during winter and in large inaccessible
35 regions has been the biggest barrier in constraining the seasonal and interannual variability of global
36 contemporary sea-air exchange (Monteiro et al. 2010; Rödenbeck et al. 2015; Bakker et al. 2016; Ritter et al.
37 2017). The increasing ship-based sampling effort and the ongoing development of autonomous observational
38 platforms (e.g. biogeochemical Argo floats and Wave Gliders) have improved confidence of interannual
39 estimates of ocean CO_2 uptake in more recent years (Monteiro et al. 2015; Bakker et al. 2016; Gray et al., 2018).

40 The community has turned to models and data-based approaches to improve estimates of CO_2 uptake by the
41 oceans for periods and regions with poor or no observational coverage (Wanninkhof et al. 2013a; Rödenbeck et
42 al. 2015; Verdy and Mazloff, 2017). Ocean biogeochemical models are able to capture the general global trend
43 in increasing oceanic CO_2 uptake shown by observations but suffer from significant regional and interannual (~ 1
44 PgC yr^{-1}) differences in their estimates because these models cannot yet accurately parameterise the marine
45 carbonate system at computationally feasible resolutions (Wanninkhof et al. 2013a). In recent years, data-based
46 approaches, namely statistical interpolations and regression methods, have become a popular alternative to
47 biogeochemical models (Lefèvre et al. 2005; Telszewski et al. 2009; Landschützer et al. 2014; Rödenbeck et al.
48 2014; Jones et al. 2015; Iida et al. 2015). The regression methods try to maximise the existing ship-based
49 observations extrapolating CO_2 using proxy variables (observable from space or interpolated). Extrapolating
50 with proxy variables is possible due to the non-linear relationship between the partial pressure of CO_2 ($p\text{CO}_2$) in
51 the surface ocean and proxies that may drive changes in surface ocean $p\text{CO}_2$. Improved access to quality
52 controlled ship-based measurements of surface ocean CO_2 through the Surface Ocean CO_2 Atlas (SOCAT)
53 database, and satellite and reanalysis products as proxy variables has aided the development of the data-based
54 methods (Rödenbeck et al. 2015; Bakker et al. 2016).

55

The current state of machine learning in ocean CO_2 estimates

56 With the increase in the number of statistical estimates of surface-ocean CO_2 , the Surface Ocean CO_2 Mapping
57 (SOCOM) community consolidated fourteen of these methods in an intercomparison of “gap-filling” methods
58 (Rödenbeck et al. 2015). The intercomparison gives an overview of the SOCOM landscape, with regression and
59 statistical interpolation approaches making up eight and four of the fourteen methods respectively (Rödenbeck et
60 al. 2015). Two model-based approaches were also compared.

61 While SOCOM intercomparison did not identify an optimal mapping method, it weighted the ensemble
62 members according to how well they represented interannual variability (IAV) relative to climatological surface



63 ocean $p\text{CO}_2$ increasing at the rate of atmospheric CO_2 concentrations (R^{jav}). Two methods, the Jena-MLS
64 (Mixed-Layer Scheme) and MPI-SOMFFN (Self-Organising Map Feed-Forward Neural-Network) were
65 weighted more due to lower R^{jav} scores. The MPI-SOMFFN (Self-Organising Map Feed-Forward
66 Neural-Network), is a global implementation of a two-step clustering-regression approach and has subsequently
67 become the most widely used method in the literature (Landschützer et al. 2015, 2016, 2018, Ritter et al. 2017).
68 The elegance of the clustering-regression approach, particularly the clustering step, is that it reduces the problem
69 into smaller parts with more coherent variability and reduces the computational size of the problem per cluster –
70 a beneficial attribute when using regression methods that do not scale well to big datasets.

71 The SOCOM intercomparison found that the gap-filling methods were in agreement in regions with a large
72 number of seasonally-resolving persistent measurements, but the different methods did not agree in regions
73 where data were sparse (e.g. the Southern Ocean).

74 **1.2 Measuring the uncertainty of estimates?**

75 The biggest limitation in assessing gap-filling methods is the paucity of data in the Southern Hemisphere
76 (Rödenbeck et al. 2015; Bakker et al. 2016). The standard use of RMSE and bias as measures of uncertainty
77 weight the regions or periods with observations heavily compared to the data-sparse regions and periods. The
78 R^{jav} score improves on the standard implementation of RMSE and bias by weighting the uncertainties annually,
79 thus giving a less temporally biased estimate of uncertainty. However, the method is still limited to the regions
80 where there are observations of $p\text{CO}_2$.

81 Previous studies have compared their methods' estimates to independent datasets, where measurements of $p\text{CO}_2$
82 are not included in the SOCAT datasets (Landschützer et al. 2013, 2014; Jones et al. 2015; Denvil-Sommer et al.
83 2018). These data serve as good validation data, particularly with the inclusion of derivations of $p\text{CO}_2$ from
84 autonomous platforms in the Southern Ocean, a historically undersampled area especially during winter (Boutin
85 and Merlivat 2013; Gray et al. 2018).

86 One of the concluding statements in the SOCOM intercomparison is that pseudo- or synthetic data
87 (deterministic model output) experiments should be used to test and compare methods. Gregor et al. (2017) did
88 just this, but their study was limited to the Southern Ocean, and the synthetic data did not fully capture the
89 variability represented by observations, in part due to coarse synthetic data resolution (5-daily mean and $1/2^\circ$
90 spatially). Moreover, such studies can only compare the limitations of the gap-filling methods within the
91 framework of the model. The authors found that the ensemble average of the compared methods outperformed
92 individual methods, in agreement with ensemble approaches previously used in ocean CO_2 studies (Khatiwala et
93 al. 2013).



94

1.3 Aims

95 The main aim of this study is to present and evaluate a new machine learning approach to estimate surface ocean
96 $p\text{CO}_2$. We propose the use of an ensemble, where we hypothesise that the “whole is greater than the sum of its
97 parts” as the strengths of the ensemble members are often complementary in such a way to overcome the
98 weaknesses (Khatiwala et al. 2013; Gregor et al. 2017). Further, we aim to evaluate the method for a selection of
99 existing gap-filling methods. From this comparison we aim not only to gain a sense of our method’s
100 performance but also the state of gap-filling based estimates; i.e. where would we be able to improve in future
101 work?
102

2 Methods

103 There are two major components to this study: surface $p\text{CO}_2$ mapping with multiple methods, robust error
104 estimation from SOCAT v5 gridded product and independent data sources. This study takes a similar two-step
105 approach used in the JMA-MLR and MPI-SOMFFN approaches, where data is grouped or clustered first, and
106 then a regression algorithm is applied to each group or cluster. We use the ocean CO_2 biomes by Fay and
107 McKinley (2014) as an option for grouping. Alongside this grouping, we use an optimal K-means clustering
108 configuration. Next, four non-linear regression methods are applied to each of the groupings. The regression
109 methods are Support Vector Regression (SVR), Feed-Forward Neural Network (FFN), Extremely Randomised
110 Trees (ERT) and Gradient Boosting Machine (GBM). The latter two approaches are new to the application.
111 These methods are then compared to independent data sources. This is outlined in more detail in the
112 Experimental Overview below.
113

2.1 Experimental overview

114 The experimental design, outlined below, is summarised in Figure 1:

- 115 1. In the first step (described by the “K-means clustering” section in Figure 1), we generate climatological
116 clusters using the oceanic CO_2 biomes by Fay and McKinley (2014), and a selection of features
117 variables (five combinations) and number of clusters (a range of clusters from 11 to 25, stepping by
118 two) resulting in a total of 41 clustering configurations.
- 119 2. Four regression algorithms are applied to each clustering configuration, resulting in 164 models
120 (described by the “Regression” section in Figure 1). The test data (isolated from model training
121 procedure) is used to identify the best performing cluster with annually weighted bias,
122 root-mean-squared error (RMSE) and R^{jav} . The four regression models for CO_2 biomes and the four
123 models from the best performing cluster and (as indicated by the bold lines in Figure 1) are used in the
124 steps that follow. The selected eight models are averaged to create an ensemble that is included with the
125 eight members for further evaluation.
- 126 3. The third step (as represented by the “K-fold testing” section in Figure 1 and Section 2.5) provides a
127 robust uncertainty evaluation based on the training data (SOCAT v5). An iterative test-train approach



- 128 is applied to estimate the bias, RMSE and R^{iav} for the complete SOCAT v5 dataset (rather than just one
129 test split).
- 130 4. The fourth step compares the ensemble estimates of surface ocean $p\text{CO}_2$ with independent test data
131 (that is not in SOCATv5, as represented by the “Independent” section in Figure 1), which allows testing
132 the predictive skill of the ensemble method (Section 2.6). Four methods from the SOCOM gap-filling
133 intercomparison study are included for reference.
- 134 5. Lastly, all gap-filling methods are compared to identify regions where there is a divergence in the trend
135 and seasonal cycle.

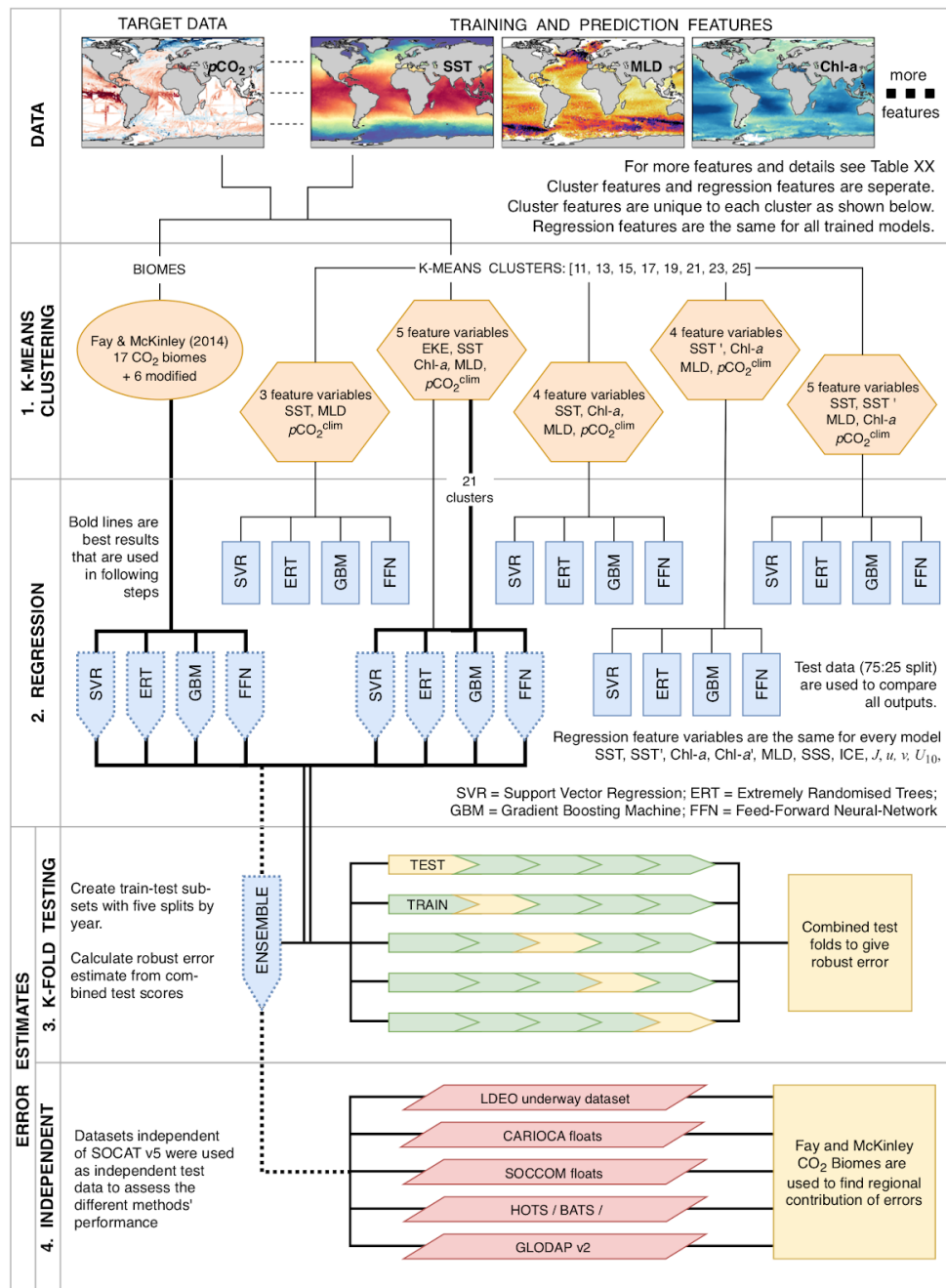
136
137
138

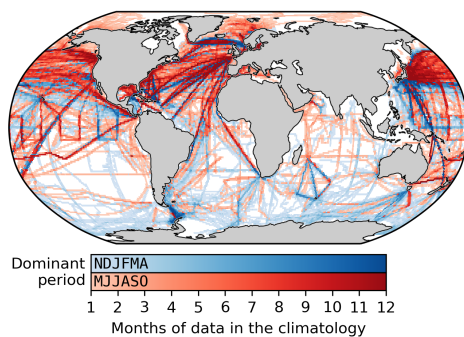
Figure 1: A flow diagram that shows the experimental procedure used in this study. Abbreviations for feature-variables in the orange hexagons can be found in Table 1. All other abbreviations are given in the diagram. Details of each step are given in the text.



139

2.2 Data: clustering, training and predictive

140 Standard machine learning implementation requires a training- and predictive dataset. The training dataset
 141 consists of a target variable that is being predicted (in this case $p\text{CO}_2$) and one or more feature-variables that
 142 have samples that correspond with target samples (*e.g.* SST, Chl-*a*, MLD co-located in space and time), where
 143 feature-variables may directly or indirectly influence the target variable. Features variables are used to predict
 144 once a machine learning model has been trained and must thus be available for the full prediction domain.



145 **Figure 2:** Map showing the distribution of the SOCAT v5 monthly gridded product (1982 to 2016) as a monthly climatology
 146 to show how well the seasonal cycle is represented (regardless of the year). The red shading shows grid-points where the
 147 majority of data occur from May to October and the blue shading shows grid-points where the majority of data occur from
 148 November to April.

149 Here we use surface ocean $p\text{CO}_2$ calculated from the SOCAT v5 monthly gridded $f\text{CO}_2$ (fugacity of CO_2)
 150 product (hereinafter SOCAT v5 as shown in Figure 2) as the target variable (Sabine et al. 2013; Bakker et al.
 151 2016). SOCAT v5 is a quality controlled dataset that contains observations of surface ocean $f\text{CO}_2$, which is
 152 converted to $p\text{CO}_2$ with:

$$p\text{CO}_2 = f\text{CO}_2 \cdot \exp(P_{\text{atm}}^{\text{surf}} \cdot \frac{B+2\delta}{R \cdot T})^{-1} \quad \text{Eq. 1}$$

153 where $P_{\text{atm}}^{\text{surf}}$ is the atmospheric pressure at the surface of the ocean, T is the sea surface temperature (SST) in
 154 °K, B and δ are virial coefficients, and R is the gas constant (Dickson et al. 2007). We used SST from the
 155 Operational Sea Surface Temperature and Sea Ice Analysis (OSTIA) product by GHRSST (Dolon et al. 2012)
 156 and ERA-interim $P_{\text{atm}}^{\text{surf}}$ (Dee et al., 2011).

157 Feature-variables in both the training and predictive datasets are globally gridded products, including satellite
 158 observations, *in-situ* measurements and reanalysis products (Table 1, see Section S1 for details). All
 159 feature-variables are gridded to a monthly frequency onto a global $1^\circ \times 1^\circ$ resolution grid. Thereafter, data
 160 processing steps are applied as shown in Table 1 and described in detail in Supplementary Materials (Section
 161 S1) with the final output being a complete dataset ranging from 1982 to 2016. Note that the clustering and
 162 regression steps use different subsets of the feature-variables as indicated in Table 1.



163
 164
 165
 166

Table 1: Summary of the products, variables and data processing steps used for feature-variables. The column “Usage” indicates the features that are used for the clustering step (identified by C) and for the regression step (identified by R). Abbreviations are used in Figure 1 and throughout the text. Basic data processing is described in the text with details in the supplementary materials (Section S1).

Group: Product	Variable	Abbrev	Usage	Processing	Reference
GHRSSST: OSTIA	Sea surface temperature	SST	C R	-	Donlon et al. (2012)
	SST seasonal anom.	SST'	C R	SST – annual average	
	Sea ice fraction	ICE	R	-	
MetOffice: EN4	Salinity	SSS	R	-	Good et al. (2013)
CDIAC: ObsPack v3	Atmospheric $p\text{CO}_2$	$p\text{CO}_2^{\text{atm}}$	R	$x\text{CO}_2^{\text{atm}} \times \text{sea level pressure}$	Masarie et al. (2014)
UCSD: Argo Mixed Layers	Mixed Layer Depth	MLD	C R	$\log_{10}(\text{climatology})$	Holte et al. (2017)
ESA: Globcolour	Chlorophyll- a	Chl- a	C R	$\log_{10}(\text{climatology filled}_{1982-1997}^{\text{cloud gaps}})$	Maritorena et al. (2010)
	Chla seasonal anom.	Chl- a'	R	Chl- a – annual average	
ECMWF: ERA-Interim 2	u -wind	u	R	-	Dee et al. (2011)
	v -wind	v	R	-	
ECMWF: ERA-Interim 2	Wind speed	U_{10}	R	$\sqrt{u^2 + v^2}$	Dee et al. (2011)
ESA: Globcurrent	Eddy kinetic energy	EKE^{clim}	C	$\log_{10}(1/2 \cdot (u'^2 + v'^2))$	Rio et al. (2014)
-	Day of the year	J	R	$\sin(\frac{i}{365}), \cos(\frac{i}{365})$	-
LDEO: $p\text{CO}_2$ climatology	Surface ocean $p\text{CO}_2$	$p\text{CO}_2^{\text{clim}}$	C	Data smoothing	Takahashi et al. (2009)

167 In this paragraph, we briefly describe the data processing steps shown in Table 1 - detailed product descriptions
 168 and in-depth processing steps are in Section S1. We derive an additional SST feature, SST', by subtracting the
 169 annual mean of SST from each respective year, leaving the annual mean anomalies (Donlon et al. 2012). We use
 170 the \log_{10} transformation of the Globcolour Chl- a global product (Maritorena et al. 2010). Cloud gaps and the
 171 period before the start of the product (1982 to 1997) are filled with the climatology (1998 – 2016), and
 172 high-latitude winter regions (where there is no climatology for Chl- a) is filled with low concentration random
 173 noise. We derive an additional Chl- a feature, Chl- a' using the same procedure as described for the SST annual
 174 mean anomalies. We use a \log_{10} transformation of mixed layer depth (MLD) from Argo float density profiles
 175 (Holte et al. 2017) to create a monthly climatology, thus imposing the assumption that there is no interannual
 176 variability. Wind speed is calculated from 6-hourly data using the equation in Table 1 before taking the monthly
 177 average. Atmospheric $p\text{CO}_2$ is calculated with: $p\text{CO}_2 = x\text{CO}_2^{\text{atm}} \times P^{\text{atm}}$, where $x\text{CO}_2^{\text{atm}}$ is the mole fraction of
 178 atmospheric CO_2 (from ObsPack v3 by Masarie et al. 2014) and P^{atm} is reanalysed mean sea-level pressure
 179 (from ERA-interim 2; Dee et al. 2011) – further details for the procedure are in the Section S1 of the
 180 Supplementary Materials. The climatology of Eddy Kinetic Energy (EKE^{clim}) is calculated from u and v surface
 181 current components (integrated for depth < 15 m) from the Globcurrent product (Rio et al., 2014), where u' is
 182 calculated as $\bar{u} - u$ and similarly with v (Table 1).

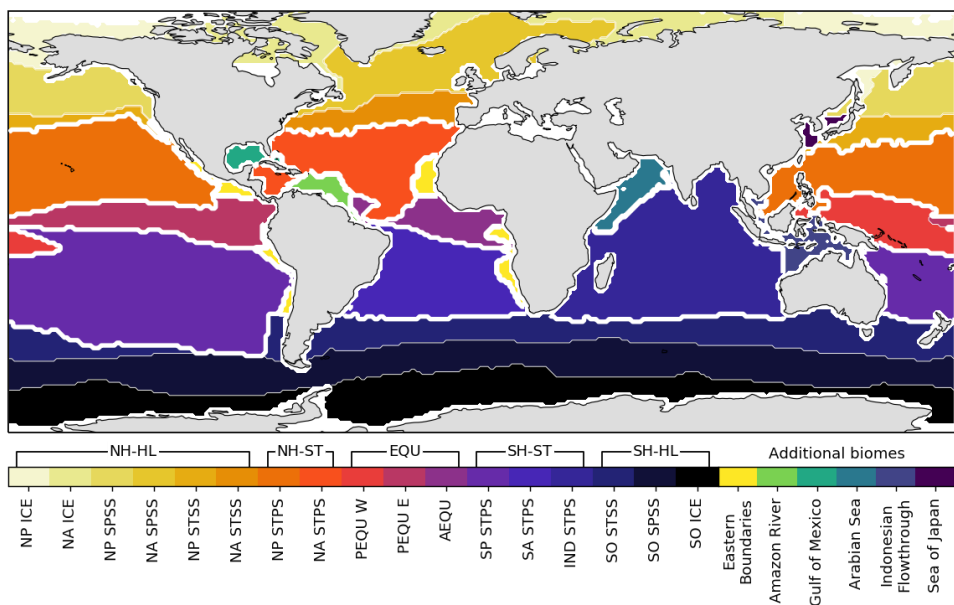


183

2.3 Clustering and biomes

184 The seasonal and interannual variability of global surface ocean $p\text{CO}_2$ is complex due to interactions of various
 185 driver variables acting on the surface ocean at different space and time scales (Lenton et al. 2012; Landschützer
 186 et al. 2015; Gregor et al. 2018). Machine learning algorithms applied globally struggle to represent the $p\text{CO}_2$
 187 accurately unless spatial coordinates are included as feature-variables (Gregor et al. 2017). A common practice
 188 is to divide the ocean into regions where processes that drive $p\text{CO}_2$ are coherent and then apply regressions to
 189 each region – five of the eight regression methods in Rödenbeck et al. (2015) apply this approach. We adopt
 190 two approaches to develop regions of internal coherence in respect of CO_2 variability.

191 Our first “clustering” approach uses the oceanic CO_2 biomes by Fay and McKinley (2014) that divide the ocean
 192 into 17 biomes. Fay and McKinley (2014) define their biomes by establishing thresholds for SST, Chl- a , sea-ice
 193 extent and maximum MLD depth. Unclassified regions from the original biomes are manually assigned based on
 194 their geographical extent resulting in six additional regions (Figure 3). Note that we may refer to the modified
 195 Fay and McKinley (2014) ocean CO_2 biomes as CO_2 biomes from here on. For later analyses, we group certain
 196 biomes together as shown by the brackets above the colour-bar in Figure (3).



197 **Figure 3:** Regions or biomes as defined by Fay and McKinley (2014). Unclassified regions from the original data have been
 198 assigned manually in this study and are shown by the separate colour palate. This modified configuration of the CO_2 biomes
 199 is referred to as BIO23 in this study. The sea-mask used in Lanschützer et al. (2014) has been applied. For the biome
 200 abbreviations (below the colour-bar) see Fay and McKinley (2014). The abbreviations above the colour-bar are used in this
 201 study, where selected biomes are grouped together. Thick white lines show the boundaries of the grouped regions. Prefixes
 202 are: NH = Northern Hemisphere, SH = Southern Hemisphere; suffixes are HL = high latitudes, ST = subtropics, and EQU =
 203 equatorial.



204 Further, we also use K-means clustering, specifically the mini-batch K-means implementation in Python's
205 Scikit-Learn package (Sculley 2010; Pedregosa et al. 2012), which is described in the supplementary materials
206 (Section S2.2; Figure S2). We apply clustering with various feature combinations and the number of clusters
207 (shown by orange hexagons in Figure 1). We tested the number of clusters ranging from 11 to 25 (stepping by
208 two). The performance of each cluster is not tested with a clustering metric; instead, we test the performance
209 based on the test scores of the regressions in the next step as a more complete indicator of performance. We find
210 optimal results in respect of RMSE and biases with 21 and 23 clusters (Figure 5). We selected 21 clusters
211 (Figure S2). Each method of defining regional coherence in respect of $p\text{CO}_2$ variability has its methodological
212 weaknesses so in this study we adopted the approach of incorporating both K-means and CO_2 biomes into the
213 ensemble (Figure 1). Although this likely weakens the geophysical meaning of the ensembled domains we
214 show that it strengthens the overall performance of the ensemble (Figure 5).

215

2.4 Regression

216 Here we describe the underlying machine learning principles of regression (*a.k.a.* supervised learning). The
217 co-located data (*i.e.* SOCAT v5) are split into training and test-subsets with a roughly 80:20 split. The test-subset
218 is isolated from the training process to attain a reliable estimate of uncertainty. We make the split between
219 training and test-subsets based on a random subset of years in the time series (1982 to 2016): 1984, 1990, 1995,
220 2000, 2005, 2010 and 2014. We avoid using a shuffled train–test split (completely random) as this leads to
221 artificially low uncertainties in machine learning algorithms that are prone to overfitting (see the experiment in
222 S2.1), where the models can reproduce the shuffled test data better as these data are adjacent to samples of the
223 same ship track.

224

Machine learning models have the ability to be as complex as the dataset at hand and are thus at risk of fitting
not only the signal but also the noise of the training data – this is known as the bias-variance tradeoff. High
variance is a result of a machine learning model that is too complex and is fitting the noise, and high bias is due
to insufficient complexity where the model cannot fit the signal (Hastie et al. 2009). Machine learning
algorithms have hyper-parameters that control the complexity of the model for each specific problem. In this
study, hyper-parameters are tuned by training the model with grid-search cross-validation, where a portion of the
training subset is iteratively kept separate from the training process for a certain set of hyper-parameters. The
hyper-parameters that result in the best score from the grid-search are used for the fit with the full training
subset. We use a variation of K-fold cross-validation called *group K-fold* in Scikit-Learn (Pedregosa et al. 2012).
Rather than having arbitrary splits for each fold, a given grouping variable is used to split the data – in this case,
years. Using years as the grouping variable reduces bias towards the second half of the time series where data is
less sparse.

236

The train-test split and cross-validation are applied identically to each of the four machine learning algorithms
for each clustering configuration. We use the following machine learning algorithms: Extremely Randomised
Trees (ERT – Geurts 2006); Gradient Boosting Machines (GBM – Friedman 2001); Support Vector Regression



239 (SVR – Drucker et al. 1997); and Feed-Forward Neural Networks (FFN). The details of these methods and how
240 they were tuned are explained in the supplementary materials (Section S2.3). The first two methods, ERT and
241 GBM, are new to this application. SVR has been implemented as a single global domain by Zeng et al. (2017),
242 and FFN is used by several different methods, some of which are in the SOCOM intercomparison (Landschützer
243 et al. 2014; Zeng et al. 2014; Sasse et al. 2013).

244 Regression performance is tested using RMSE primarily but also bias (Equations 3 and 4) and R^{av} (Equation 5)
245 with only the models from the best averaged cluster used for the rest of the study.

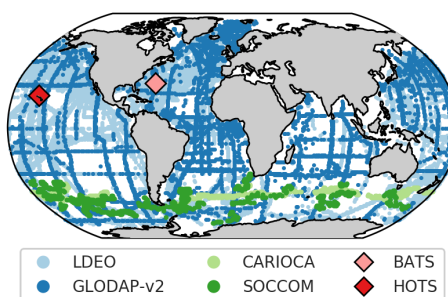
246 **2.5 Robust biases and root-mean-square errors**

247 Standard practice in machine learning is to set aside a test-subset of the data as described in Section 2.4. We use
248 this standard approach in the second step of our experiment as an estimate of the performance for each of the
249 machine learning models (164 in total). However, this grouped train-test split gives a bias and RMSE estimate
250 limited to the random test years of test-subset (see Section 2.4). To overcome this limitation, we apply the
251 train-test split method five times in a K-fold-like test approach (Figure 1: “K-fold testing” section), meaning that
252 the data in a test fold is never used to train the model. The splits in the test fold are also based on a subset of
253 years spaced five years apart. We then refactor the five test-fold estimates into a complete test-estimate (with the
254 same structure as the original SOCAT v5), thus giving a complete estimate of bias and RMSE. This robust
255 test-estimate method ensures that correct biases and RMSE scores are reported even if methods are prone to
256 overfitting (see Section S2.1 and Figure S1). We limit this procedure to only the CO₂ biome and best cluster
257 regressions as it has five times the computational cost of a single train-test split.

258

2.6 Method validation data

259 For method validation we use observation data that are not used in SOCAT (Figure 4 and Table 2) as they are
260 either: 1) included in LDEO, but not SOCAT; 2) not measured with an infrared analyser; 3) derived from two
261 other variables in the marine carbonate system, where these include dissolved inorganic carbon (DIC), pH and
262 total alkalinity (TA) – SOCCOM floats use empirically calculated TA.



263 **Figure 4:** The distribution of the validation data. Details of these datasets are given in Table 2. HOTS and BATS are marked
264 as diamonds to distinguish them as time series stations.



265 **Table 2:** Details for the validation datasets. The measured variables are shown (DIC = dissolved inorganic carbon; TA = total
 266 alkalinity) along with the estimated accuracy of $p\text{CO}_2$. This includes the propagated uncertainty in the conversion from DIC
 267 and TA to $p\text{CO}_2$ as defined by Lueker et al. (2000), where the estimates marked with * are an extrapolation of the estimates
 268 as the DIC and TA uncertainties do not match or exceed those listed in the publication. Grid points show the number of data
 269 at the same resolution as the feature-variables.

Platform	Project	Measured variable	Accuracy (μatm)	Reference	Grid points
Ship	LDEO	$p\text{CO}_2$ Equilibrator	$\pm 2.5 \mu\text{atm}$	Takahashi et al. (2016)	16161
	GLODAP v2	DIC + TA	$\sim 12 \mu\text{atm} @ 400 \mu\text{atm} ^*$	Olsen et al. (2016)	5976
Surface floats	CARIOCA	$p\text{CO}_2$ Colourimetric	$\pm 3.0 \mu\text{atm}$	Boutin and Merlivat (2013)	613
Profiling floats	SOCOMM	pH + TA (LIAR)	$\sim 11 \mu\text{atm} @ 400 \mu\text{atm}$	Carter et al. (2016)	1037
Mooring	BATS	DIC + TA	$\sim 4 \mu\text{atm} @ 400 \mu\text{atm}$	Bates (2007)	246
	HOTS	DIC + TA	$< 7.6 \mu\text{atm} @ 400 \mu\text{atm} ^*$	Dore et al. (2009)	214

270 The uncertainty of $p\text{CO}_2$ that is calculated from DIC and TA is dependent on the accuracy of these two
 271 measurements, as well as the derivation of $p\text{CO}_2$ with dissociation constants, for which we use the *CBSys*
 272 package in Python (Hain et al. 2015). *CBSys* implements the constants from Lueker et al. (2000) that reports an
 273 uncertainty of 1.9% standard deviation of the calculated $p\text{CO}_2$ where DIC and TA uncertainties are 2.0 and 4.0
 274 $\mu\text{mol}\cdot\text{kg}^{-1}$ respectively. The measurements in GLODAP v2 are slightly larger than this at 4 and 6 $\mu\text{mol}\cdot\text{kg}^{-1}$,
 275 which would result in an error larger than 1.9% – this is 12 μatm for a 400 μatm estimate at a hypothetical 3%
 276 error. While this potentially large error range may seem concerning, we argue that the inclusion of these data in
 277 data-sparse regions is more valuable than their omission. Moreover, the errors from the previous gap-filling
 278 products are on the order of 20 μatm , below the potential uncertainty from the DIC/TA conversion to $p\text{CO}_2$
 279 (Landschützer et al. 2014; Rödenbeck et al. 2014). Williams et al. (2017) estimated the error for $p\text{CO}_2$ calculated
 280 empirically to be 2.7%, where TA was calculated empirically with the Locally Interpolated Alkalinity
 281 Regression (LIAR) algorithm (Carter et al. 2016). All $p\text{CO}_2$ data are then gridded to the same time and space
 282 resolution as the feature-variables (monthly \times 1°) using *xarray* and *pandas* packages in Python (McKinney,
 283 2010; Hoyer and Hamman, 2017).

284

2.7 Sea-air CO_2 flux calculation

285 Sea-air CO_2 flux ($F\text{CO}_2$) is calculated with:

$$F\text{CO}_2 = K_0 \cdot k_w \cdot (p\text{CO}_2^{\text{sea}} - p\text{CO}_2^{\text{atm}}) \quad \text{Eq. 2}$$

286 where K_0 is the solubility of CO_2 in seawater (Weiss 1974) and k_w is the gas-transfer velocity calculated from
 287 wind speed using formulation by Wanninkhof et al. (2013). We scale k_w so that the global mean is 16 cm hr^{-1} ,
 288 following the same procedure as Landschützer et al (2014). $p\text{CO}_2^{\text{sea}}$ is from the gap-filling methods, and $p\text{CO}_2^{\text{atm}}$
 289 is atmospheric $p\text{CO}_2$. All ancillary variables required in these calculations are the same as those listed in Table 1,
 290 except for $p\text{CO}_2^{\text{atm}}$, which is the CarboScope atmospheric $p\text{CO}_2$ product from Rödenbeck et al. 2014.

291

2.8 Relative interannual variability and interquartile range metrics

2.8.1 Regression metrics

293 We use bias and root-mean-square error (RMSE) as first-order metrics of model performance.



294 Bias is the mean difference between the target variable and the estimates thereof:

$$Bias = \sum_{i=1}^n \frac{\hat{y}_i - y_i}{n} \quad \text{Eq. 3}$$

295 where n is the number of training samples, y is the array of target data and \hat{y} is the corresponding array of
 296 estimates. Similarly, RMSE is a measure of the difference between the target variable and the estimates thereof:

$$RMSE = \sqrt{\sum_{i=1}^n \frac{(y_i - \hat{y}_i)^2}{n}} \quad \text{Eq. 4}$$

297 In our study, these metrics are calculated for each year and then the mean of the annual bias or RMSE scores is
 298 taken as a more robust measure of performance in the context of temporally imbalanced data. This is typically
 299 done for the global domain unless otherwise stated.

300 The relative interannual variability metric (R^{iav}) was introduced by Rödenbeck et al. (2014) and used in the
 301 SOCOTM intercomparison by Rödenbeck et al. (2015) to measure how well a method represents the interannual
 302 variability of SOCAT v5. The metric furthers the idea of RMSE calculated by year (and region if stated,
 303 otherwise global) by normalising annually weighted RMSE to a benchmark with minimal interannual and
 304 seasonal variability:

$$R^{iav} = \frac{\sigma_{1982-2015}(M^{iav(t)})}{\sigma_{1982-2015}(M_{bench}^{iav})} \quad \text{Eq. 5.1}$$

$$M^{iav(t)} = \sqrt{\sum_{i=1}^n \frac{(y_i - \hat{y}_i)^2}{n-1}} \quad \text{Eq. 5.2}$$

$$M_{bench}^{iav} = \sqrt{\sum_{i=0}^{n-1} \frac{(y_i - \hat{y}_i^b)^2}{n-1}} \quad \text{Eq. 5.3}$$

305 Here σ is the standard deviation of M^{iav} and M_{bench}^{iav} respectively, which are both represented as yearly time
 306 series. Equations 5.2 and 5.3 show the formulation for $M^{iav(t)}$ and M_{bench}^{iav} , which represent these metrics for a
 307 single year. The symbol i represents individual data points in a particular year t , y is the observation-based data
 308 for that year, \hat{y} is the predicted data and n is the number of points in the year and region. The benchmarked
 309 M_{bench}^{iav} is calculated to normalise M^{iav} . The \hat{y}^b represents the data that has been corrected for IAV by subtracting
 310 the climatology and atmospheric pCO_2 trend from the predictions.

311

2.8.2 Ensemble metrics

312 We use the interquartile range (IQR) between different gap-filling methods as a robust metric of disagreement,
 313 where the standard deviation is sensitive to outliers. IQR is calculated as the third quartile (75th percentile) minus
 314 the first quartile (25th percentile). The disagreement between methods is calculated with interannually resampled
 315 data and then averaged over the time series to arrive at the interannual disagreement (IQR^{IA}). This is calculated
 316 per pixel if the representation of the data is spatial (maps) and per time step of a time series.

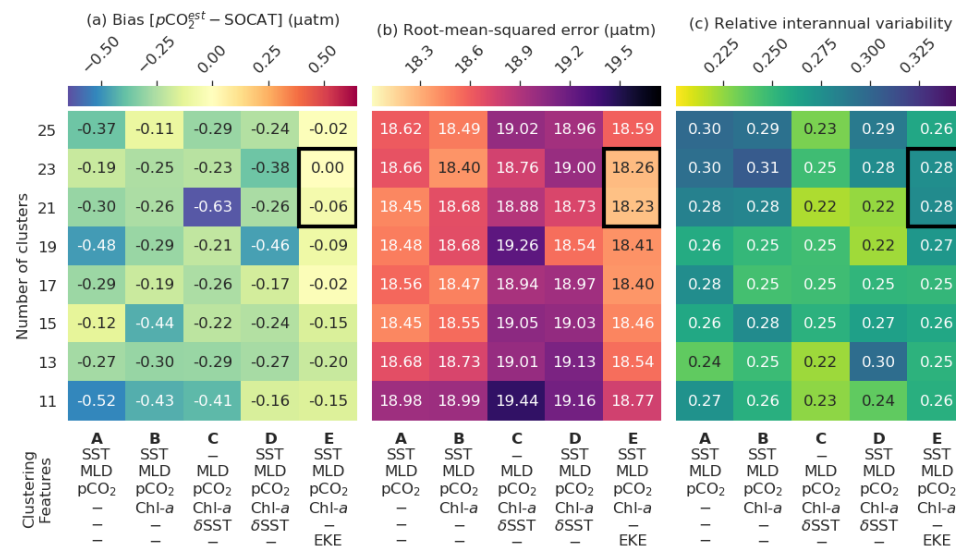


317

3 Results

318 3.1 Regression results

319 The results from the second part of the experiment (as shown in Figure 1) are depicted in Figure (5a-c) which
 320 plots the matrix of the (a) average bias, (b) RMSE and (c) R^{iav} for each combination of the experimental number
 321 of clusters and clustering features. The RMSE and bias are calculated by averaging the annual estimates for the
 322 randomly selected test years (as explained in Section 2.4) rather than using the entire dataset - this is done to
 323 minimise the effect of the temporal imbalance in the number of observations.



324 **Figure 5:** Heatmaps showing the average cluster (a) bias, (b) root-mean-squared error (RMSE) and (c) relative interannual
 325 variability (R^{iav}) for different cluster configurations, where smaller scores are better for all metrics. The rows show the
 326 number of clusters, and the columns show clustering feature-variable configurations. Each cluster contains the average of
 327 scores for four regression methods: support vector regression, extremely randomised trees, gradient boosting machine,
 328 and feed-forward neural-network. The black box indicates clustering configurations that perform well across all metrics – note
 329 that a $R^{iav} < 0.3$ falls within the best category of performance in Rödenbeck et al. (2015).

330 Results show that the configuration that includes EKE^{clim} (column E in Figure 5a-c) as a clustering feature has
 331 the lowest average RMSE and absolute bias for nearly all clusters, regardless of the number of clusters (rows in
 332 Figure 5a,b). The increased dynamics associated with high EKE regions might change the way pCO_2 behaves
 333 compared to low EKE regions (Monteiro et al. 2015; du Plessis, 2017, 2019). The optimal number of clusters
 334 within this configuration is either 21 or 23, based on the smallest bias and RMSE scores (as indicated by the
 335 black box in Figure 5). Note that we do not weight R^{iav} strongly in this assessment as a R^{iav} score of less than 0.3
 336 is in the top performing category in the SOCOTM intercomparison (Roddenbeck et al. 2015). We select the
 337 configuration with the lowest RMSE, which has 21 clusters with the following features: SST, $\log_{10}(MLD^{clim})$,



338 $p\text{CO}_2^{\text{clim}}$, $\log_{10}(\text{Chl-}a^{\text{clim}})$, and $\log_{10}(\text{EKE}^{\text{clim}})$; and is hereinafter abbreviated as K21E (see Figure S2 for the
 339 distribution of the climatology for these clusters).

340 Comparatively, the Fay and McKinley (2014) CO_2 biomes have an average RMSE score of 18.98 μatm (Table 3)
 341 but have a lower mean R^{iav} (0.26) and smaller bias (0.03 μatm) than the K21E configuration. Given that the CO_2
 342 biomes perform well and provide an alternate clustering approach, we include the regression estimates
 343 (hereinafter we refer to the Fay and McKinley (2014) CO_2 biomes with the six additional biomes as BIO23).
 344 The eight machine learning models from K21E and BIO23 (four each) were used to create an ensemble by
 345 averaging $p\text{CO}_2$ estimates (CSIR-ML8).

346 **Table 3:** Regression scores for the CO_2 biomes (BIO23), the cluster configuration from column E in Figure 5 (K21E) and the
 347 ensemble (CSIR-ML8). Abbreviations are: RMSE = root-mean-square error; R^{iav} = relative interannual variability (Equation
 348 5). Regression methods are: SVR = support vector regression; ERT = extremely randomised trees; GBM = gradient boosting
 349 machine; FFN = feed-forward neural-network. Bold values are significantly lower than the mean for that column ($p < 0.05$
 350 for two-tailed Z-test; absolute values used for bias column).

Cluster	Regression	Bias (μatm)	RMSE (μatm)	R^{iav}
CSIR-ML8		0.04	17.25	0.25
K21E	SVR	-0.45	17.95	0.24
	ERT	0.84	17.96	0.36
	GBM	-0.32	18.21	0.24
	FFN	-0.30	18.82	0.27
BIO23	SVR	-0.19	18.47	0.15
	ERT	0.85	18.76	0.38
	GBM	0.02	19.05	0.28
	FFN	-0.58	19.65	0.21

351 All regression methods have lower RMSE scores for K21E than for BIO23, but R^{iav} and bias do not indicate that
 352 any of the two clustering approaches is preferable (Table 3). Comparing the RMSE scores of the individual
 353 regression methods, we see that the model scores are ranked the same in each cluster from first to last: SVR,
 354 ERT, GBM, FFN. However, it is important to note that this ranking does not apply to bias or R^{iav} , where ERT has
 355 low RMSE, but the largest bias and R^{iav} in each cluster. CSIR-ML8 outperforms nearly all its members with
 356 RMSE and bias scores of 17.25 μatm and 0.04 μatm respectively. However, the ensemble R^{iav} (0.25) is only just
 357 less than the average of the ensemble members' average (0.26).

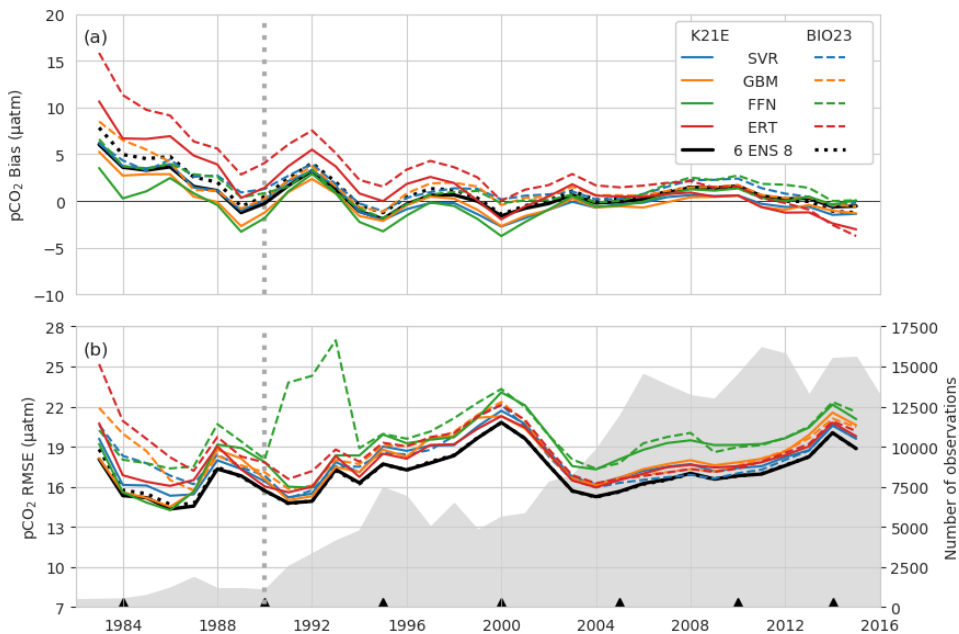
358

3.2 Robust RMSE, bias and R^{iav}

359 Here, we study the change in the bias and RMSE for all selected methods (i.e. K21E, BIO23 and CSIR-ML8;
 360 Table 3) across 1982-2016 (Figure 6). Most notable is that bias scores for all models have the same interannual
 361 tendencies, with a positive bias at the beginning of the time series (1982 to 1993) that is strongest before 1990,
 362 strongly influencing the mean bias (Table 4). Secondly, the biases for K21E (solid lines) are, on average, smaller



363 than for BIO23 (dashed lines) as shown for the annually averaged results in Table 4 ($0.73 \mu\text{atm}$ and $2.24 \mu\text{atm}$
 364 respectively). These biases are much larger than those reported in Table 3 (with averages of absolute biases of
 365 $0.48 \mu\text{atm}$ and $0.41 \mu\text{atm}$ for K21E and BIO23 respectively), but this is likely since selected test years (black
 366 triangles in Figure 6b) fall on years of low bias. While FFN has the largest RMSE ($18.93 \mu\text{atm}$ and $20.24 \mu\text{atm}$
 367 for K21E and BIO23), it has a smaller bias compared to other regression methods ($0.04 \mu\text{atm}$ and $1.60 \mu\text{atm}$
 368 respectively), motivating for including FFN regressions in the ensemble (Table 4). Conversely, the ERT
 369 approach has a significant positive bias ($2.08 \mu\text{atm}$ and $3.88 \mu\text{atm}$ for K21E and BIO23 respectively, with $p >$
 370 0.95 for both values; Table 4). A second ensemble without ERT regressions, thus with six members
 371 (CSIR-MLR6 version 2019a, hereafter called CSIR-ML6), has lower biases compared to CSIR-ML8 ($0.98 \mu\text{atm}$
 372 and $1.48 \mu\text{atm}$ respectively; Table 4).



373 **Figure 6:** Annually averaged (a) bias and (b) RMSE for the eight individual regression methods in Table 3: BIO23 (dashed
 374 lines) and K21E (solid lines). The dotted black lines show the ensemble averages for all eight models (CSIR-ML8), and the
 375 solid black line shows metrics for the ensemble of the SVR, GBM and FFN (CSIR-ML6) from BIO23 and K21E. The grey
 376 filled area in (b) shows the number of observations per year and black triangles show the years that are isolated as the test
 377 subset. The vertical dashed grey line demarks 1990 prior to which there is a large positive bias.

378 Similarly to the biases, RMSE for all models (Figure 6b) have similar interannual tendencies and variability,
 379 with a sharp peak in the year 2000 ($> 20 \mu\text{atm}$ where the mean RMSE is $18.61 \mu\text{atm}$). The increased RMSE
 380 scores are likely due to the spatial distribution of sampling (see Figure S3), e.g. an increase in sampling in the
 381 high latitudes during spring and summer, a region and period of high variability and biogeochemical complexity,
 382 would increase the weight of these data in the final RMSE calculation, thus resulting in larger RMSE scores.
 383 The increase in the number of samples from 2002 to 2016 results in a sharp decrease in RMSE ($< 19 \mu\text{atm}$ for
 384 the majority of this period). Both ensembles outperform all other methods for the majority of the time series



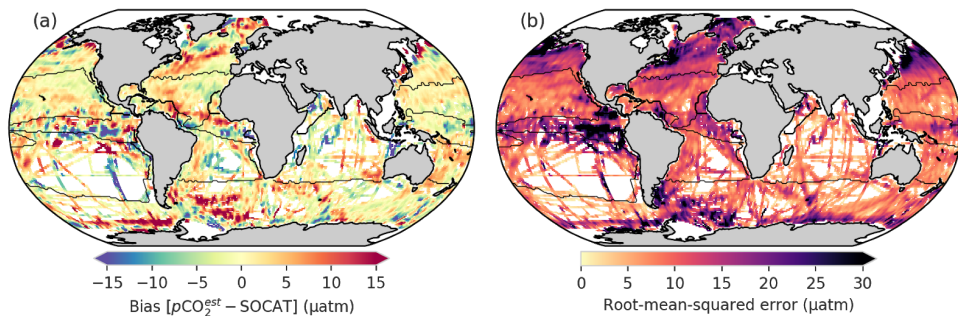
385 with RMSE scores of 17.16 μatm and 17.25 μatm for CSIR-ML6 and CSIR-ML8 respectively (see Table S1
 386 comparisons of ensembles with different members).

387 The R^{iav} scores for the robust errors (Table 4) are lower than train-test results with a single split reported in Table
 388 3, likely due to an increase of standard deviation for the IAV benchmark (Equation 5). The lowest score is held
 389 by CSIR-ML6 (0.20) and is lower (better) than the average for its members (0.21). These R^{iav} estimates compare
 390 well to the Jena-MLS and SOM-FFN, which both scored < 0.3 (Rödenbeck et al. 2015).

391 **Table 4:** The robust estimates of bias, RMSE and R^{iav} from 1982 to 2016 for BIO23, K21E and the ensemble averages,
 392 CSIR-ML6 and CSIR-ML8, where the first excludes the ERT. Bold values are significantly lower than the mean for that
 393 column ($p < 0.05$ for two-tailed Z-test; absolute values used for bias column). See Table S1 for further comparisons between
 394 different ensemble configurations.

Cluster	Regression	Bias (μatm)	RMSE (μatm)	R^{iav}
CSIR	ML6	0.98	17.16	0.20
	ML8	1.48	17.25	0.22
K21E	SVR	0.58	18.04	0.21
	ERT	2.08	18.20	0.27
	GBM	0.21	18.05	0.21
	FFN	0.04	18.93	0.22
BIO23	SVR	1.76	18.17	0.21
	ERT	3.88	19.16	0.32
	GBM	1.72	18.59	0.21
	FFN	1.60	20.24	0.21

395 The spatial distribution of the bias and RMSE is now studied for the CSIR-ML6 ensemble (Figure 7 a and b,
 396 respectively), particularly focusing on the regional patterns emerging from the data. CSIR-ML6 clearly
 397 represents the subtropical regions (NH-ST and SH-ST) with relatively low biases and RMSE scores ($< |5 \mu\text{atm}|$
 398 and $10 \mu\text{atm}$ respectively). The equatorial regions (EQU), especially the eastern Pacific, contrasts this with large
 399 uncertainties in both bias and RMSE ($> |10 \mu\text{atm}|$ and $30 \mu\text{atm}$ respectively). The high-latitude oceans (NH-HL
 400 and SH-HL) have considerable uncertainties due to the large interannual variability of surface ocean $p\text{CO}_2$
 401 caused by the formation and retreat of sea-ice (around Antarctica; Ishii et al. 1998; Bakker et al. 2008) and
 402 phytoplankton spring blooms (Atlantic sector of the Southern Ocean, North Pacific and Arctic Atlantic;
 403 Thomalla et al. 2011; Lenton et al. 2013; Gregor et al. 2018). There are two bands of overestimates on the
 404 southern and northern boundaries of the North Atlantic Gyre, where the latter coincides with the Gulf Stream.
 405 Regression approaches may be prone to a positive bias in the North Atlantic as this was also shown by
 406 Landschützer et al. (2013; 2014).



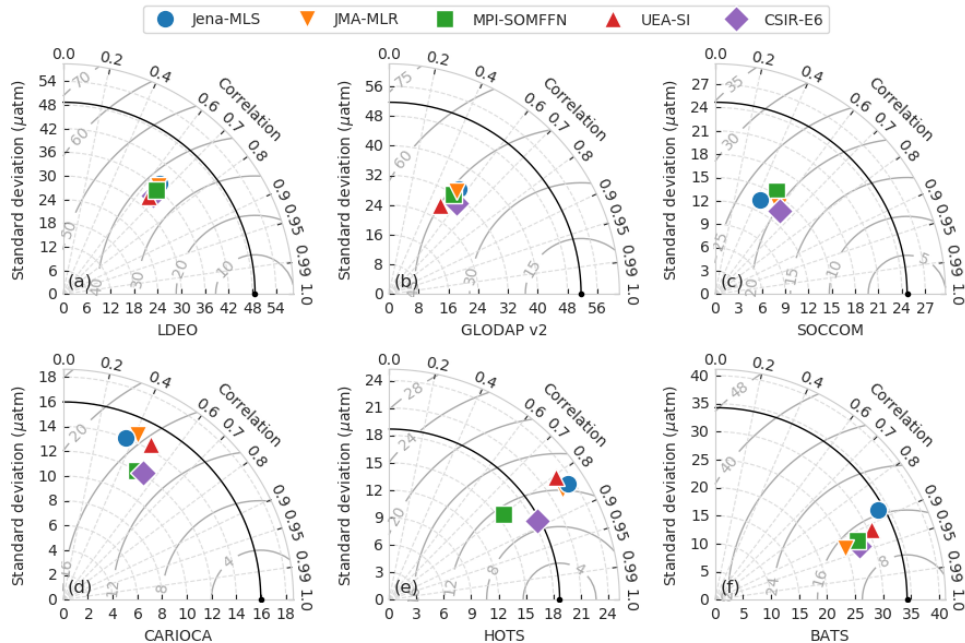
407 **Figure 7:** (a) shows the biases from the robust test-estimates; (b) shows the root-mean-squared errors for CSIR-ML6. A
 408 convolution has been applied to (a) and (b) to make it easier to see the regional nature of the biases and RMSE. Figure S4
 409 shows the bias for every ensemble member.

410 In summary, the robust test-estimates show that there is a bias positive bias in $p\text{CO}_2$ predictions before 1990 for
 411 all models, but is largest for ERT and excluding these models from the ensemble results in better $p\text{CO}_2$
 412 predictions. The spatial evaluation of the performance metrics for CSIR-ML6 shows that regions with specific
 413 oceanic features (e.g. western boundary currents) mostly have positive biases. However, it is important to note
 414 that these uncertainty assessments are limited as the characteristics and biases of the dataset are intrinsic to the
 415 models. Validation with independent data is thus a more reliable estimate of the performance of these methods.
 416

3.3 Validation with independent datasets

417 Here, we validate the accuracy of $p\text{CO}_2$ estimates from CSIR-ML6 with independent data (that is not in SOCAT
 418 v5 as described in Table 2). To further study the behaviour of our ensemble estimates relative to previous
 419 studies, we compare the results from four independent methods of the SOCOM intercomparison project against
 420 the independent data (Rödenbeck et al. 2015). Those four independent methods are: the Jena mixed-layer
 421 scheme (Jena-MLS version *oc_v1.6*, Rödenbeck et al. 2014); Japanese Meteorological Agency – multi-linear
 422 regression (JMA-MLR updated on 2018-12-2, Iida et al. 2015); Max Planck Institute – Self-organising Map
 423 Feed-forward Neural-network (MPI-SOMFFN v2016, Landschützer et al. 2017); and University of East Anglia
 424 – Statistical Interpolation (UEA-SI version 1.0, Jones et al. 2015). $p\text{CO}_2$ estimates by the Jena-MLS were
 425 resampled to monthly temporal resolution and interpolated to a one-degree grid using Python’s *xarray* package.

426 The performance of each gap-filling method is represented with a Taylor diagram for each independent
 427 validation dataset (Figure 8; Taylor et al. 2001). The most important characteristic learnt from these plots is that
 428 the gap-filling methods are tightly bunched for nearly all validation datasets, indicating a similar RMSE,
 429 correlation and standard deviation relative to the reference datasets. Poor estimates in Figures 8a-d may indicate
 430 that the training data for gap-filling methods is the limiting factor. Secondly, the gap-filling methods almost
 431 always underestimate the standard deviation of the validation datasets, being below the black arced line for all
 432 but HOTS (Figure 8e).



433 **Figure 8:** Taylor diagrams comparing the $p\text{CO}_2$ estimates of five gap-filling methods with validation datasets (Table 2), for
434 the period 1990–2015. Each validation dataset has its own Taylor diagram as labelled on the bottom axes. The black marker
435 on the bottom axis in each subplot represents the validation dataset and the black arc shows the standard deviation thereof.
436 The closer that the gap-filling estimates are to this point, the better the model's performance, in terms of variance, centred
437 RMSE and correlation (for bias information, see Table 5). The solid grey arcs show the centred RMSE for the datasets (with
438 bias removed).

439 All methods fail to represent the standard deviation of the two global validation datasets, LDEO and GLODAP
440 v2 (Figures 8a,b), with centred RMSE scores greater than 35 μatm . However, calculating RMSE annually results
441 in scores of $\sim 27 \mu\text{atm}$ for LDEO and $\sim 35 \mu\text{atm}$ for GLODAP v2, much lower than shown in Figure 8a,b due to
442 high RMSE scores ($> 40 \mu\text{atm}$) for a small subset of years (Section S3.3 and Figure S54). Estimates of the
443 Southern Ocean datasets (Figures 8c, d), SOCCOM and CARIOLA, have lower RMSE scores ($\sim 16 \mu\text{atm}$ and
444 $\sim 23 \mu\text{atm}$ respectively) relative to LDEO and GLODAP v2. However, for standard deviation scores of similar
445 magnitude and low correlation coefficients, the datasets are not well constrained (Table 5). The SOCCOM
446 dataset also has the largest average absolute bias for estimates, with gap-filling methods underestimating by at
447 least 11 μatm (Table 5). This large bias may be because SOCCOM floats have a proportionately large number of
448 winter samples – suggesting that our knowledge of Southern Ocean winter fluxes are largely underestimated
449 (Williams et al. 2017). In contrast, all methods estimate the two time-series stations, HOTS and BATS (Figures
450 8e,f and Table 5) relatively well with correlation scores of > 0.8 and low average bias $\sim 4.5 \mu\text{atm}$.



451
 452
 453
 454

Table 5: The RMSE and bias for each gap-filling method compared to the validation datasets. For more information on the validation-datasets see Table 2. The first row of data (count) shows the number of gridded samples in the dataset during the period 1990–2015 (that are not in the SOCAT v5 gridded product). Values shown in bold are significantly different from the mean for the column ($p < 0.05$ for two-tailed Z-test; absolute values used for biases).

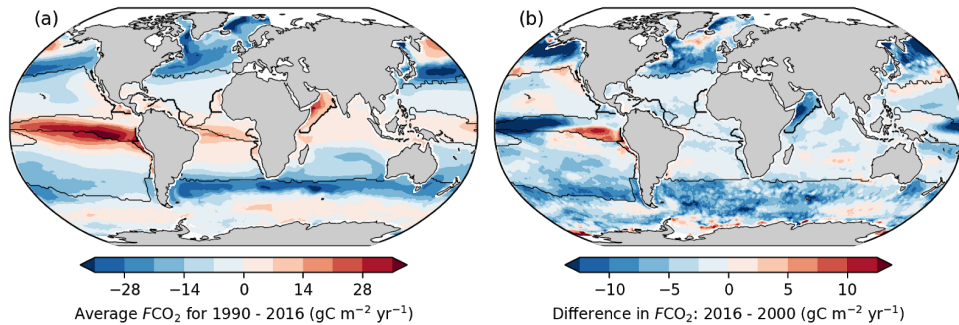
Metric	Method	LDEO	GLODAP-v2	SOCCOM	CARIOCA	BATS	HOTS
Count	Count	16161	5976	1037	613	246	214
RMSE	CSIR-ML6	26.55	32.84	23.15	14.26	12.53	8.62
	MPI-SOMFFN	27.43	35.96	25.21	15.08	13.39	10.40
	JMA-MLR	29.11	34.53	22.32	16.05	14.29	11.64
	Jena-MLS	27.61	35.52	26.83	18.24	16.14	12.28
	UEA-SI	27.35	35.07		15.73	13.35	18.52
Bias	CSIR-ML6	-1.18	8.48	-13.12	4.28	0.32	0.46
	MPI-SOMFFN	-0.19	9.16	-13.79	4.00	-1.41	-0.12
	JMA-MLR	-1.86	6.62	-11.25	2.85	-3.98	2.22
	Jena-MLS	-0.14	8.48	-14.68	7.18	4.09	6.15
	UEA-SI	-0.71	9.20		0.79	-2.02	16.27

455 Despite all scores being closely grouped (Figure 8), Table 5 shows that the CSIR-ML6 method scores
 456 significantly lower RMSE scores (using a two-tailed Z-test with $p < 0.05$) for all but one of the datasets
 457 (SOCCOM). However, bunching of the RMSE scores (Figure 8) is beneficial with regard to achieving low
 458 p -values. No single method dominates the biases, with JMA-MLR and MPI-SOMFFN each scoring the lowest
 459 bias on two occasions. To summarise, all gap-filling methods underperform when validated against independent
 460 observational products. Tight bunching of gap-filling method scores per validation dataset shows that training
 461 data may limit all methods in the same manner.

462

3.4 The effect of uncertainties on the sea-air CO₂ flux interannual variability

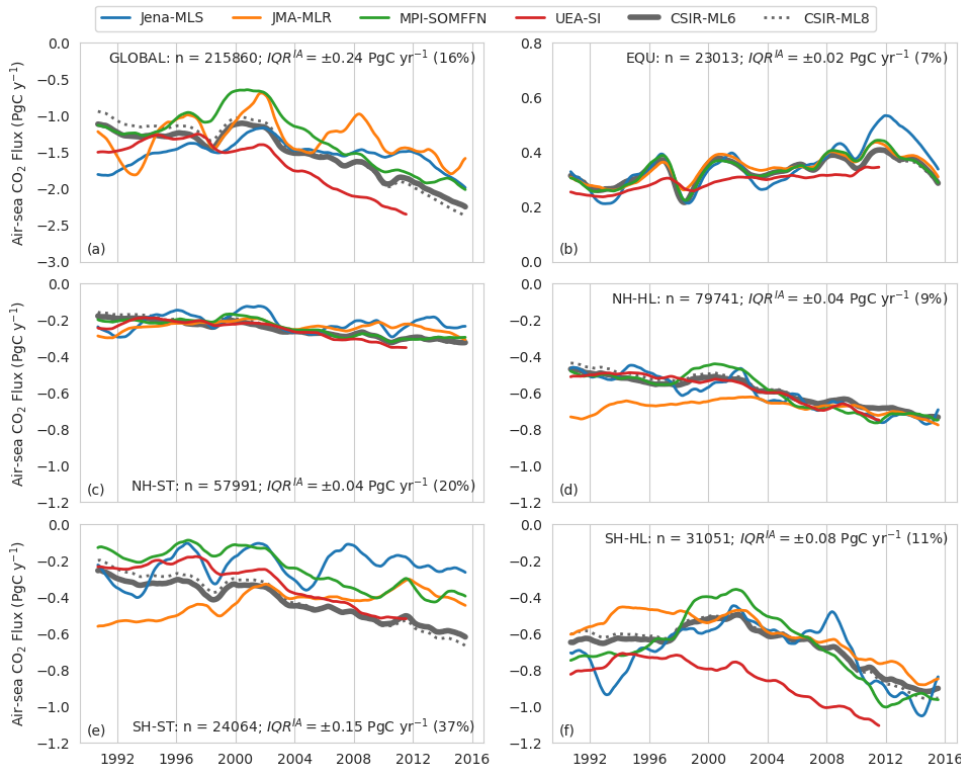
463 In this section, we assess the regional implications of the differences in gap-filling methods' estimates of the
 464 sea-air CO₂ flux (F_{CO_2}) over the period 1990 to 2016. F_{CO_2} was calculated using the same gas transfer velocity
 465 and solubility for each gap-filling method (Section 2.7). Differences in F_{CO_2} are thus driven by variations in
 466 pCO_2 from each gap-filling method.



467 **Figure 9:** (a) Average sea-air CO_2 fluxes (FCO_2) of CSIR-ML6 for 1990 to 2016, where FCO_2 is calculated as shown in
 468 Equation 2. Negative FCO_2 (blue) indicates regions of atmospheric CO_2 uptake. (b) The difference between FCO_2 in 2016
 469 and 2002, which are the minimum and maximum of global ocean uptake flux (FCO_2) estimates respectively (for CSIR-ML6
 470 in Figure 10a). Black lines show the regions as defined in Figure 2.

471 The average FCO_2 for 1990-2016 by CSIR-ML6 (Figure 9a) contextualises the regional distribution of fluxes:
 472 strong outgassing in the Equatorial Pacific, strong sink in the mid-latitudes, a moderate uptake for the most part
 473 of the subtropics, and weak source in the majority of the Southern Ocean (in agreement with e.g. Takahashi et
 474 al., 2009). The global annual time-series for FCO_2 as simulated by CSIR-ML6 (Figure 10a) indicates a
 475 strengthening for 2000 to 2016 (as for the other methods). To give spatial context to this strengthening, we
 476 display the differences in FCO_2 between 2016 and 2000 (Figure 9b), since those are the two years where the
 477 difference in global FCO_2 is greatest for CSIR-ML6 (Figure 10a). Note that Figure 9b serves as a snapshot for
 478 the change in FCO_2 between those two years, whose interpretation cannot be linked to an overall
 479 anthropogenically-forced change as the comparison between two years could highlight interannual, decadal or
 480 multi-decadal variability. The differences in FCO_2 between 2016 and 2000 is negative in the high latitudes and
 481 moderately positive in the subtropics, indicating a respective increase and decrease in the CO_2 ocean uptake
 482 between the two years. The Eastern Equatorial Pacific is the only region that shows a considerable increase in
 483 FCO_2 ($> 10 \text{ gC m}^{-2} \text{ yr}^{-1}$) between the two specific years.

484 The annual change in FCO_2 is also studied for the different regions. The Southern Hemisphere high-latitude
 485 (SH-HL) region is the strongest contributor to the trend (Figure S6b), where there is a steady increase in the
 486 uptake of CO_2 since the 2000s for all methods (Landschützer et al. 2015; Gregor et al. 2018). On average, the
 487 Northern Hemisphere high latitudes (NH-HL) are a weaker sink relative to the SH-HL, because the SH-HL is
 488 more than double the area of the NH-HL (Figure S6c). The equatorial (EQU) region is the only persistent source
 489 of CO_2 to the atmosphere (also seen in Figure 9a). The subtropical regions (Figure 10c, e) contribute to global
 490 flux on similar orders of magnitude; however, there is a large divergence between gap-filling methods in the
 491 SH-HL.



492 **Figure 10:** Sea-air CO_2 fluxes averaged for regions as shown in Figure 2: (a) global domain, (b) Equatorial regions,
 493 (c) Northern Hemisphere Subtropical, (d) Northern Hemisphere High Latitude, (e) Southern Hemisphere Subtropical, (f)
 494 Southern Hemisphere High Latitude. The coloured lines show the four SOCOM products. The thick and dotted grey lines
 495 show the results for CSIR-ML6 and CSIR-ML8, respectively. A moving average of 12 months has been applied to smooth
 496 the data. Note that the y-axes scales differ for the top (a) and (b). The text at the right of each figure shows the number of
 497 SOCAT v5 gridded data points for each region (n) and the inter-annual interquartile range (IQR^{IA}).
 498

498 We use the average interquartile range between the one-year rolling mean estimates (IQR^{IA}) as a measure of
 499 agreement or divergence between gap-filling methods, where large values indicate a divergence (Section 2.8.2).
 500 We also show the IQR^{IA} scaled to the range of the regional interannual variability (max – min) as a percentage
 501 ($\text{relative IQR}^{\text{IA}}$), which shows if the trend for a particular region is agreed on by all methods (the smaller the
 502 percentage, the better the agreement across methods). The disagreement between methods in the SH-ST is
 503 substantial (Figure 10e), with diverging $F\text{CO}_2$ throughout the period with an IQR^{IA} of 0.15 PgC yr^{-1} and a very
 504 large relative IQR^{IA} of 37%. Similarly, the IQR^{IA} for the SH-HL region (Figure 10f) is 0.08 PgC yr^{-1} , but the
 505 relative IQR^{IA} is much lower at 11%, indicating that all methods agree on the observed strong trend. Compared
 506 to the Southern Hemisphere, the Northern Hemisphere regions are both relatively well constrained, with IQR^{IA}
 507 estimates of 0.04 PgC yr^{-1} for both regions (Figure 10c,d). However, a large relative IQR^{IA} of 20% suggests that
 508 the interannual $F\text{CO}_2$ estimates in this region are potentially not resolving the trend, or more likely that there is a

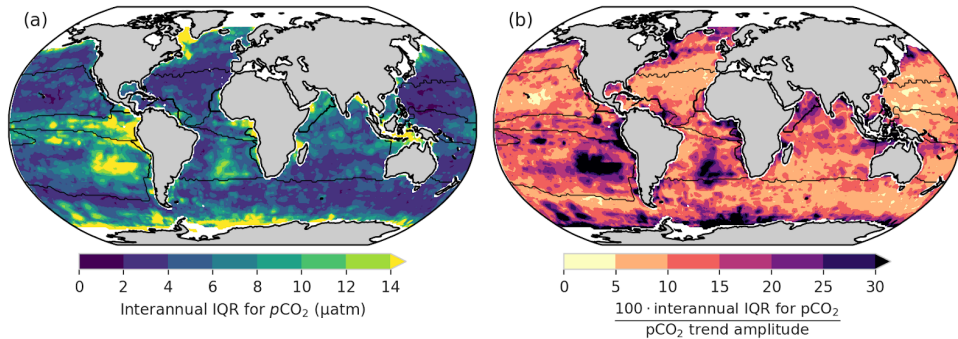


509 weak trend with a small difference between the minimum and maximum interannual estimates of FCO_2 . The
510 equatorial region (EQU - Figure 10b) has the lowest IQR^{IA} and relative score at 0.02 PgC yr⁻¹ and 7%.

511 The CSIR-ML8 method is not included in the IQR^{IA} calculations but is included in Figure 10 to show the impact
512 of the ERT models' positive bias in pCO_2 on FCO_2 (Figure 6a). The biases are positive at the beginning and
513 negative end of the time series, with the average absolute difference between the CSIR methods being 0.08 PgC
514 yr⁻¹. The positive biases have the strongest impact in the SH-ST that occupies 36% total area (Figure S6c), with
515 only 11% of the total observations in SOCAT, suggesting that this method is sensitive to imbalanced datasets.
516

3.5 Regional disagreement between methods

517 In order to better understand the regional distribution of the uncertainties in FCO_2 , we assess the level of
518 agreement between methods in their interannual surface ocean pCO_2 estimates (Figure 11). We use pCO_2 for this
519 representation as no spatial integration occurs – only time averaging.



520 **Figure 11:** (a) The magnitude of the interannual disagreement between gap-filling methods (IQR^{IA}). (b) Level of agreement
521 on the interannual variability across methods, more specifically IQR^{IA} scaled by the difference between the maximum and
522 minimum values for interannual pCO_2 (the range).

523 The interannual estimates of interquartile range (IQR^{IA} ; Figure 11a) show the disagreement between methods is
524 relatively small in the majority of the ocean ($\approx 5 \mu\text{atm}$); the exceptions being the South Atlantic, southeastern
525 Pacific and eastern equatorial Pacific with differences of $> 10 \mu\text{atm}$. The IQR^{IA} scaled to the
526 maximum-minimum range of interannual pCO_2 suggests that the NH-ST is well constrained (< 10%), which is
527 in conflict with the IQR^{IA} for FCO_2 in Figure 10c (where the relative IQR^{IA} is 20%). The disagreement may stem
528 from the magnifying impact that wind speed has on FCO_2 , *i.e.* small differences in pCO_2 may become large
529 when fluxes are calculated. The same principle may apply to the EQU in Figure 11b, where relative IQR^{IA} is
530 large ($> 10 \%$) for pCO_2 , but low wind speeds result in a low relative IQR^{IA} for FCO_2 (7% in Figure 10b). The
531 largest relative IQR^{IA} scores occur in the SH-ST ($> 10\%$ in Figure 11c) where data is sparse, specifically the
532 South Atlantic and southeastern Pacific (Figure 2a). The relative IQR^{IA} scores suggest that the gap-filling
533 methods agree on pCO_2 in the SH-HL east of the Greenwich meridian ($> 0^\circ \text{E}$).



534 In summary, we show that there is an agreement between gap-filling methods in the Northern Hemisphere for
535 interannual $p\text{CO}_2$, but the methods show considerable disagreement in the Southern Hemisphere, particularly in
536 the subtropics. Disagreements in the Equatorial and Southern Hemisphere high-latitude regions are large (>
537 10%) and should be treated with caution when considering trends in these regions.
538

4 Discussion

539 4.1 Not all models are equal

540 In their study, Khatiwala et al. (2013) stated that: “*our comparison of different methods suggests, that multiple*
541 *approaches, each with its own strengths and weaknesses, remain necessary to quantify the ocean sink of*
542 *anthropogenic CO₂*”. In our study, we embrace this philosophy by creating an ensemble of two-step machine
543 learning models that estimate global surface ocean $p\text{CO}_2$. The authors of the SOCOM intercomparison
544 (Rödenbeck et al. 2015) warn against the use of ensembles with the statement: “*We also discourage any*
545 *ensemble averaging (or medians, etc.) of full spatiotemporal fields or time series, as this would result in*
546 *variations that are not self-consistent any more and fit the data less well than individual products*”. Our
547 approach may seem in opposition to the statement, but we show robustly that the CSIR-ML6 method reproduces
548 the available data with greater accuracy than previous methods, albeit in an incremental way. Our method is
549 methodologically consistent with regard to feature-variables. Though there is variability in the clustering and the
550 regression, we create the ensemble with a good understanding of each model’s biases (Figure 6 and Figure S4).
551 The argument that ensembles reduce transparency is also somewhat diminished by the fact that little additional
552 information that can be gained from highly non-linear models, with the exception of basic diagnostics such as
553 feature-variable importance (see Figure S7) from decision-tree-based approaches (Pedregosa et al. 2012;
554 Castelvecchi, 2016). Our results thus show that there is, in fact, a benefit in creating an ensemble of models
555 (Table 5), and if carefully implemented is an additional tool that can be used to reduce the uncertainties in
556 gap-filling estimates of $p\text{CO}_2$.

557 It could be argued that an exhaustive search for the optimal configuration (Figure 5) for CSIR-ML6 may result
558 in poorly trained individual models. However, we think that the merit of introducing and assessing regression
559 algorithms new to the application (for gradient boosting machines and extremely randomised trees) outweighs
560 the marginal loss in potential performance for individual methods. Moreover, lessons learnt from our study can
561 be used to improve on future iterations. It also makes the case for ensembles stronger as the CSIR-ML6
562 performs well relative to other gap-filling methods.

563 In the search for the optimal clustering configuration (Figure 5a,b), we show that including EKE (along with
564 SST) as a clustering feature-variable leads to an improvement in bias and RMSE for nearly all number of
565 clusters. Increased intra-seasonal variability of $p\text{CO}_2$ appears to be associated with regions of high EKE
566 compared to low EKE regions (Monteiro et al. 2015; du Plessis, 2017, 2019). Moreover, the importance of EKE

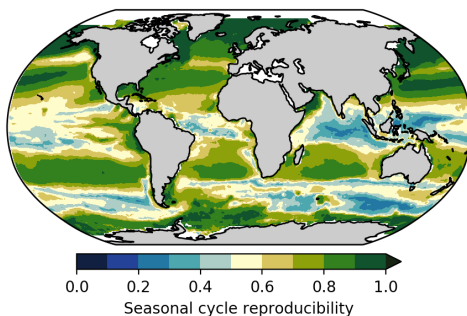


567 as a part of the cluster constraints also shows that more thought should be given to how we sample $p\text{CO}_2$ in
568 high-EKE regions and at what resolution regression methods are run at – we discuss this in detail later.

569 Our findings suggest the following about the individual regression methods: the SVR and GBM algorithms
570 produce good estimates with lower RMSE scores and biases, the FFN approach has larger RMSE scores yet low
571 biases than the other methods, and the ERT approach has low RMSE scores but large biases in the estimates
572 (Figure 6a,b; Table 4). We do not include the ERT approach in the ensemble (CSIR-ML6) due to the large
573 time-evolving biases, suggesting that ERT (with our tuning) is not suitable for estimating surface ocean $p\text{CO}_2$.
574 The bias in ERT may be due to its sensitivity to imbalanced datasets (Crone and Finlay, 2012), where the data in
575 SOCAT v5 are few before 2000. Returning to the above quote by Khatiwala et al. (2013), we thus find that the
576 weaknesses of ERT outweigh its strengths.
577

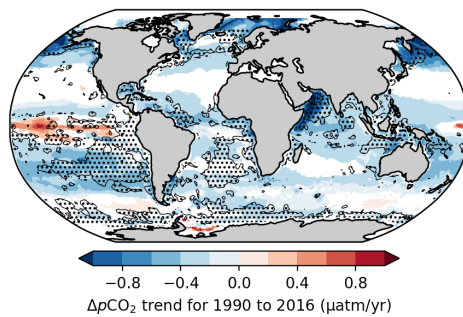
4.2 Divergent gap-filling estimates

578 While we see that the improvements in the performance of gap-filling methods are relatively stagnant (relative
579 to the training and validation data), the differences between the methods' estimates of $p\text{CO}_2$ and FCO_2 vary
580 significantly in some regions particularly in regions where data is sparse such as in the Southern Hemisphere
581 oceans (Figure 2). We also find that training the gap-filling methods with limited training data exposes the
582 intrinsic biases of the algorithms, or in the words of Ritter et al. (2017): “*the difference [between ga-filling
583 methods] is a result of how the spatial and seasonal heterogeneity and the sparseness of the data is dealt with*”.
584 Conversely, as the number of training data increase, the biases are reduced, and the methods converge.



585 **Figure 12:** The seasonal cycle reproducibility of CSIR-ML6 $p\text{CO}_2$, which is a correlation of detrended $p\text{CO}_2$ with its own
586 climatology – the larger the correlation the stronger the reproducibility of the seasonal cycle (method from Thomalla et al.
587 2011).

588 The Northern Hemisphere subtropical regions are a good example of a region where the gap-filling methods
589 converge (Figure 11b), as also shown by the low RMSE scores and high correlation for the two mooring
590 stations, HOTS and BATS (Figure 8e,f). One of the reasons that the methods can predict the variability well in
591 the subtropics (Figure 8e,f) is because these regions are less biogeochemically complex and driven primarily by
592 seasonal changes in SST (Bates 2001; Dore et al. 2009). This strong SST-driven seasonality in the subtropics is
593 shown by the high seasonal cycle reproducibility (Figure 12).



594 **Figure 13:** $\Delta p\text{CO}_2$ trends ($p < 0.05$), where $\Delta p\text{CO}_2$ is calculated as the estimated surface ocean $p\text{CO}_2$ from the
595 CSIR-ML6 method minus atmospheric $p\text{CO}_2$ from the CarboScope project (Rödenbeck et al. 2014). The shaded areas
596 show the regions where $\text{IQR}^{\text{IA}} > 15\%$, thus indicating regions where trends should be interpreted with caution.

597 The gap-filling methods' divergences also serve as a metric to inform where there is not enough data to
598 constrain the $p\text{CO}_2$ or $F\text{CO}_2$ estimates, *i.e.* the divergences inform us where estimates should be treated with
599 caution. The IQR^{IA} , when scaled to the range of the interannual variability (Figure 11b), should be taken into
600 account when analysing interannual trends of $\Delta p\text{CO}_2$ (Figure 13). For instance, trend estimates in $\Delta p\text{CO}_2$ for
601 CSIR-ML6 are negative ($p < 0.05$) for the majority of the global ocean, even in regions where method estimates
602 are too disparate to resolve interannual variability (relative $\text{IQR}^{\text{IA}} > 15\%$; Figure 13). However, the relative
603 IQR^{IA} is not without its limits, as there may be regions where methods are in agreement but share the same
604 biases, thus reporting false confidence in the estimates. Regions of false confidence would most likely occur in
605 data sparse areas, but could only truly be identified with better data coverage in these regions.
606

4.3 Inching up and over the wall: incremental improvements

607 In our study, we show that all gap-filling methods suffer from the same uncertainties where there are data to test
608 and validate the estimates (Figure 8), and divergences between estimates when there are insufficient data to
609 constrain the methods (Figure 11b). From these points, it may seem that we may have in fact "hit the wall" in
610 terms of better resolving surface ocean $p\text{CO}_2$. In this section, we discuss how we might overcome this proverbial
611 wall. First, by first addressing the uncertainty and biases within the methods, and then discussing the issue of
612 data scarcity, specifically, how could we most effectively improve our sampling strategies to close the gaps in
613 the current datasets.
614

4.3.1 Reducing systematic errors

615 The robust test-estimates show that there are regions where training data is not sparse, yet estimates still suffer
616 from large uncertainties (*e.g.* northern and southern boundaries of the North Atlantic gyre in Figure 7a,b and
617 Figure S4). These errors are spatially consistent with those reported by Landschützer et al. (2014). Such regional
618 mismatches between gridded observations and estimates are likely systematic – meaning that gap-filling
619 methods are not able to resolve the more complex $p\text{CO}_2$ variability at current resolutions (monthly $\times 1^\circ$ or



620 coarser) or with the current regression feature-variables (Gregor et al. 2017; Denvil-Sommer et al. 2018). It may
621 be possible to reduce these uncertainties with consideration about the drivers of CO₂ in a specific region.

622 Including appropriate additional feature-variables (if available), such as reanalysis mixed-layer depth products,
623 may improve the uncertainties of gap-filling methods (Gregor et al. 2017). Similarly, increasing the temporal
624 and spatial resolution may be able to improve estimates where aliasing occurs in regions of high dynamic
625 variability such as the mid-latitude oceans (Monteiro et al. 2015). It is worthwhile noting that increasing the
626 resolution may not be the panacea for poor estimates. For example, the Jena-MLS method is able to estimate
627 *p*CO₂ with relative accuracy (Figure 8) at a low spatial ($\approx 4^\circ \times 5^\circ$; Rödenbeck et al. 2014); however, with the
628 trade-off in spatial resolution, the method is able to increase the temporal resolution to 6-hourly estimates.

629 One of the weaknesses of our study is that our approach is similar to other clustering-regression methods,
630 namely MPI-SOMFFN and JMA-MLR, which could lead to similar biases between these clustering-regression
631 methods. Importantly, this highlights the need for new methods that are fundamentally different and may lead to
632 the development of procedural architectures that might be able to resolve the biases in well-sampled regions
633 better. For example, a recent study by Denvil-Sommer et al. (2018) developed a method (LSCE-FFNN) that first
634 estimates the climatological *p*CO₂ and then the anomalies from this climatology – their method reported RMSE
635 scores on the order of those reported in this study ($\sim 18.0 \mu\text{atm}$) and very low R^{jav} scores (< 0.2). While new
636 methods might not lead to drastic reductions in uncertainties, incremental improvements in uncertainties will be
637 driven by approaches that offer new solutions, whether it be increased resolution, additional feature-variables or
638 a new approach.

639 4.3.2 Scale-sensitive sampling strategies

640 All gap-filling methods suffer from similar biases and uncertainties (Figure 8, Table 5) when compared to
641 independent validation data, yet the same methods show vastly different results in data-sparse regions. These
642 shared uncertainties and regionally-consistent divergences between methods suggest that insufficient training
643 data is the limiting factor (Rödenbeck et al. 2015; Landschützer et al. 2016; Ritter et al. 2017; Denvil-Sommer et
644 al. 2018). Our study highlights the need for targeted sampling in these data-sparse regions, with the relative
645 IQR^{1A} metric (Figures 11b) providing a guideline of where sampling should occur to better resolve interannual
646 *p*CO₂. Large mismatches in the Southern Hemisphere subtropics and the Southern Ocean suggest that these
647 remote regions require more data to be constrained.

648 Autonomous sampling platforms, such as biogeochemical Argo floats, surface drifters and wave gliders, are
649 offering a new and efficient way to target inaccessible regions with relative affordability at the scales required to
650 resolve not only interannual but also intraseasonal variability (e.g. Monteiro et al. 2015). Despite being
651 potentially less accurate than the SOCAT requirements, including these measurements might still result in
652 improved *p*CO₂ estimates as long as measurements are not positively or negatively biased (Wanninkhof et al.
653 2013b).



654 While autonomous platforms offer a low-cost solution to improve data coverage in data-sparse regions, there
655 needs to be a better understanding of the required sampling rates to resolve $p\text{CO}_2$ at any given location and
656 season - scale sensitivity question – a point that also addresses the issue of increasing the resolution of
657 gap-filling methods. Observing system simulation experiments (OSSEs) offer useful insight into the required
658 sampling density and frequency (Lenton et al. 2006, Lenton et al. 2009, Majkut et al. 2014; Mazloff et al. 2018;
659 Kamenkovich et al. 2011, 2017). The majority of these OSSEs have been focussed on resolving fluxes in the
660 Southern Ocean, which perhaps deserves the attention as it is the largest contributor to interannual $F\text{CO}_2$
661 variability (Figure S6b; Landschützer et al. 2016). Another Southern Ocean study found that a sampling rate of
662 at least three days was required to resolve intraseasonal variability in a region with high dynamic variability
663 such as the SH mid-latitude oceans (Monteiro et al. 2015) – a much higher sampling rate than the 10-day period
664 for carbon (pH)-enabled Argo floats.

665 Finally, over and above the focus of recent work on the Southern Ocean, there seems to be a gap in the
666 community's efforts in reducing the uncertainties in the Southern Hemisphere subtropical oceans – a region with
667 few observations (Figure 2) and significant disagreement between methods (Figure 10). Importantly, the eastern
668 Pacific and eastern Indian oceans may be more variable than their well sampled Northern Hemisphere
669 counterparts as suggested by the spatial autocorrelation length-scales of $p\text{CO}_2$ (for where there are
670 measurements) and satellite proxies (SST, Chl- a and sea surface height; Jones et al. 2012). And while the
671 gap-filling methods estimate that there is high seasonal cycle reproducibility in these regions (Figure 12;
672 meaning that gap-filling methods might well resolve them), we do not have enough information about the
673 carbon cycle in these regions to make these assumptions. If anything, this should be an encouragement to the
674 community that these undersampled regions can easily be resolved, especially with the use of autonomous
675 sampling platforms.

676

5 Summary

677 Our study suggests that we may be reaching the limits of gap-filling methods' abilities to reduce uncertainties,
678 as shown by the limited incremental improvement in errors by the ensemble method we compare with
679 established methods. Significant uncertainties still prevail across all gap-filling methods, most likely limited by
680 the extent of basin-scale observational gaps in the Southern Hemisphere as well as sampling aliases in
681 mesoscale intensive ocean regions. We propose ways in which the surface ocean CO_2 community can improve
682 estimates within the bounds of the current observations, and make recommendations for future observations.

683 We introduce a new surface ocean $p\text{CO}_2$ gap-filling method that is a machine learning ensemble of six two-step
684 clustering-regression models (CSIR-ML6 version 2019a). An exhaustive search process was used to find the
685 best K-means clustering configuration which was used alongside the Fay and McKinley (2014) oceanic CO_2
686 biomes. The regression models applied to each clustering method are support vector regression, feed-forward
687 neural-networks and gradient boosting machines. We show that the ensemble of the six methods outperforms



688 each of its members, thus promoting the idea that averaging model estimates, each with different strengths and
689 weaknesses, results in an improvement in the overall estimates.

690 The CSIR-ML6 (version 2019a) ensemble approach was compared to validation data alongside four other
691 methods from the SOCOM intercomparison study (Rödenbeck et al. 2015). Our new method marginally
692 outperformed the SOCOM methods when comparing RMSE scores for the validation data, but fared equally on
693 biases. Despite this improvement, all methods had errors of roughly the same magnitude, suggesting that the
694 methods are resolving $p\text{CO}_2$ equally outside the bounds of the training data.

695 Closer assessment of the spatial distribution of errors shows that there is spatial coherence between regression
696 approaches for the Northern Hemisphere. Some of these errors coincide with regions of high dynamic variability
697 or complex biogeochemistry, suggesting that increasing the spatial and temporal resolution of gap-filling
698 methods could improve estimates. Moreover, introducing additional feature-variables for regression, such as
699 eddy kinetic energy, may improve estimates in these regions.

700 A comparison of the spatial distribution of mismatches in $p\text{CO}_2$ between gap-filling methods shows that there
701 are regions (primarily in the Southern Hemisphere) where the compared methods, as an ensemble, cannot
702 resolve interannual variability of $p\text{CO}_2$. These large mismatches are likely to occur due to amplification of
703 methodological biases in data-sparse areas. We propose that scale-sensitive integrated multi-platform sampling
704 of $p\text{CO}_2$ in these regions should be the top priority for the community - a task that is made easier by the
705 development of autonomous sampling platforms. Moreover, we suggest that optimised simulation sampling
706 experiments should be used to understand the spatial and temporal requirements of $p\text{CO}_2$ in different regions and
707 periods.

708 In closing, we suggest that it is time to consider another SOCOM-like intercomparison. Several new methods
709 have been developed since the last intercomparison and the addition of these would improve the robustness of
710 ensemble flux estimates. Further, the authors of the SOCOM intercomparison suggest that a future
711 intercomparison should include a comparison of methods using simulated data, a method to overcome the
712 limitation of the lack of data to test the estimates.

713

Code and data availability

714 Supporting code is available in Supplementary Materials. Data (global surface ocean $p\text{CO}_2$ from CSIR-ML6
715 version 2019a) is available at <https://doi.org/10.6084/m9.figshare.7894976.v1>.

716

Author contributions

717 LG is the lead author and developed the method and wrote the manuscript. ADL contributed to the model
718 assessment and contributed in editing the manuscript. SK contributed to the initial conceptualisation of the



719 methods and proofread the manuscript. PMSM contributed to the development of the manuscript and its
720 reviews.
721

Acknowledgements

722 This work is part of a Post-doctoral research fellowship funded by the CSIR's Southern Ocean Carbon - Climate
723 Observatory (SOCCO) through financial support from the Department of Science and Technology (DST) and
724 the National Research Foundation (NRF) and hosted at the MaRe Institute at UCT. We acknowledge the support
725 from the Centre for High Performance Computing (CSIR-CHPC). The Surface Ocean CO₂ Atlas (SOCAT) is an
726 international effort, endorsed by the International Ocean Carbon Coordination Project (IOCCP), the Surface
727 Ocean Lower Atmosphere Study (SOLAS) and the Integrated Marine Biogeochemistry and Ecosystem Research
728 program (IMBER), to deliver a uniformly quality-controlled surface ocean CO₂ database. The many researchers
729 and funding agencies responsible for the collection of data and quality control are thanked for their contributions
730 to SOCAT.
731

References

- Bakker, D. C. E., Hoppema, M., Schr, M., Geibert, W. and Baar, H. J. W. De: A rapid transition from ice covered CO₂-rich waters to a biologically mediated CO₂ sink in the eastern Weddell Gyre, *Biogeosciences*, 5, 1373–1386, 2008.
- Bakker, D. C. E., Pfeil, B., Landa, C. S., Metzl, N., O'Brien, K. M., Olsen, A., Smith, K., Cosca, C., Harasawa, S., Jones, S. D., Nakaoka, S., Nojiri, Y., Schuster, U., Steinhoff, T., Sweeney, C., Takahashi, T., Tilbrook, B., Wada, C., Wanninkhof, R. H., Alin, S. R., Balestrini, C. F., Barbero, L., Bates, N. R., Bianchi, A. A., Bonou, F., Boutin, J., Bozec, Y., Burger, E. F., Cai, W.-J., Castle, R. D., Chen, L., Chierici, M., Currie, K., Evans, W., Featherstone, C., Feely, R. A., Fransson, A., Goyet, C., Greenwood, N., Gregor, L., Hankin, S., Hardman-Mountford, N. J., Harley, J., Hauck, J., Hoppema, M., Humphreys, M. P., Hunt, C. W., Huss, B., Ibánhez, J. S. P., Johannessen, T., Keeling, R., Kitidis, V., Kötzinger, A., Kozyr, A., Krasakopoulou, E., Kuwata, A., Landschützer, P., Lauvset, S. K., Lefèvre, N., Lo Monaco, C., Manke, A., Mathis, J. T., Merlivat, L., Millero, F. J., Monteiro, P. M. S., Munro, D. R., Murata, A., Newberger, T., Omar, A. M., Ono, T., Paterson, K., Pearce, D., Pierrot, D., Robbins, L. L., Saito, S., Salisbury, J., Schlitzer, R., Schneider, B., Schweitzer, R., Sieger, R., Skjelvan, I., Sullivan, K. F., Sutherland, S. C., Sutton, A. J., Tadokoro, K., Telszewski, M., Tuma, M., Van Heuven, S. M. A. C., Vandemark, D., Ward, B., Watson, A. J. and Xu, S.: A multi-decade record of high-quality fCO₂ data in version 3 of the Surface Ocean CO₂ Atlas (SOCAT), *Earth Syst. Sci. Data*, 8(2), 383–413, doi:10.5194/essd-8-383-2016, 2016.
- Bates, N. R.: Interannual variability of oceanic CO₂ and biogeochemical properties in the Western North Atlantic subtropical gyre, *Deep. Res. Part II Top. Stud. Oceanogr.*, 48(8–9), 1507–1528, doi:10.1016/S0967-0645(00)00151-X, 2001.
- Boutin, J. and Merlivat, L.: Sea surface fCO₂ measurements in the Southern Ocean from CARIOCA Drifters, , doi:10.3334/CDIAC/OTG.CARIOCA, 2013.
- Carter, B. R., Feely, R. A., Williams, N. L., Dickson, A. G., Fong, M. B. and Takeshita, Y.: Updated methods for global locally interpolated estimation of alkalinity, pH, and nitrate, *Limnol. Oceanogr. Methods*, 16(2), 119–131, doi:10.1002/lom3.10232, 2018.
- Castelvecchi, D.: Can we open the black box of AI?, *Nature*, 538(7623), 20–23, doi:10.1038/538020a, 2016.
- Crone, S. F. and Finlay, S.: Instance sampling in credit scoring: An empirical study of sample size and balancing, *Int. J. Forecast.*, 28(1), 224–238, doi:10.1016/j.ijforecast.2011.07.006, 2012.
- Dee, D. P., Uppala, S. M., Simmons, A. J., Berrisford, P., Poli, P., Kobayashi, S., Andrae, U., Balmaseda, M. A., Balsamo, G., Bauer, P., Bechtold, P., Beljaars, A. C. M., van de Berg, L., Bidlot, J., Bormann, N., Delsol, C., Dragani, R.,



Fuentes, M., Geer, A. J., Haimberger, L., Healy, S. B., Hersbach, H., Holm, E. V., Isaksen, L., Kallberg, P., Köhler, M., Matricardi, M., Menally, A. P., Monge-Sanz, B. M., Morcrette, J. J., Park, B. K., Peubey, C., de Rosnay, P., Tavolato, C., Thépaut, J. N., Vitart, F., Hólm, E. V., Källberg, P. and Thépaut, J. N.: The ERA-Interim reanalysis: Configuration and performance of the data assimilation system, *Q. J. R. Meteorol. Soc.*, 137(656), 553–597, doi:10.1002/qj.828, 2011.

Denvil-Sommer, A., Gehlen, M., Vrac, M. and Mejia, C.: FFNN-LSCE: A two-step neural network model for the reconstruction of surface ocean pCO₂ over the Global Ocean, *Geosci. Model Dev. Discuss.*, (November), 1–27, doi:10.5194/gmd-2018-247, 2018.

Dickson, A. G. (Andrew G., Sabine, C. L., Christian, J. R. and North Pacific Marine Science Organization.): Guide to best practices for ocean CO₂ measurements, North Pacific Marine Science Organization. [online] Available from: <https://www.oceanbestpractices.net/handle/11329/249> (Accessed 16 February 2019), 2007.

Donlon, C. J., Martin, M., Stark, J., Roberts-Jones, J., Fiedler, E. and Wimmer, W.: The Operational Sea Surface Temperature and Sea Ice Analysis (OSTIA) system, *Remote Sens. Environ.*, 116, 140–158, doi:10.1016/j.rse.2010.10.017, 2012.

Dore, J. E., Lukas, R., Sadler, D. W., Church, M. J. and Karl, D. M.: Physical and biogeochemical modulation of ocean acidification in the central North Pacific, *Proc. Natl. Acad. Sci.*, 106(30), 12235–12240, doi:10.1073/pnas.0906044106, 2009.

Drucker, H., Burges, C. J. C., Kaufman, L., Smola, A. and Vapnik, V. N.: Support vector regression machines, *Adv. Neural Inf. Process. Syst.* 9, 1, 155–161, doi:10.1111.10.4845, 1997.

du Plessis, M., Swart, S., Ansorge, I. J. and Mahadevan, A.: Submesoscale processes promote seasonal restratification in the Subantarctic Ocean, *J. Geophys. Res.*, 122(4), 2960–2975, doi:10.1002/2016JC012494, 2017.

du Plessis, M., Swart, S., Ansorge, I. J., Mahadevan, A. and Thompson, A. F.: Southern Ocean seasonal restratification delayed by submesoscale wind-front interactions, *J. Phys. Oceanogr.*, JPO-D-18-0136.1, doi:10.1175/JPO-D-18-0136.1, 2019.

Fay, A. R. and McKinley, G. A.: Global open-ocean biomes: Mean and temporal variability, *Earth Syst. Sci. Data*, 6(2), 273–284, doi:10.5194/essd-6-273-2014, 2014.

Friedman, J. H.: Greedy function approximation: A gradient boosting machine, *Ann. Stat.*, 29(5), 1189–1232, doi:10.1214/aos/1013203451, 2001.

Geurts, P., Ernst, D. and Wehenkel, L.: Extremely randomized trees, *Mach. Learn.*, 63(1), 3–42, doi:10.1007/s10994-006-6226-1, 2006.

Good, S. A., Martin, M. J. and Rayner, N. A.: EN4: Quality controlled ocean temperature and salinity profiles and monthly objective analyses with uncertainty estimates, *J. Geophys. Res. Ocean.*, 118(12), 6704–6716, doi:10.1002/2013JC009067, 2013.

Gray, A. R., Johnson, K. S., Bushinsky, S. M., Riser, S. C., Russell, J. L., Talley, L. D., Wanninkhof, R. H., Williams, N. L. and Sarmiento, J. L.: Autonomous Biogeochemical Floats Detect Significant Carbon Dioxide Outgassing in the High-Latitude Southern Ocean, *Geophys. Res. Lett.*, 45(17), 9049–9057, doi:10.1029/2018GL078013, 2018.

Gregor, L., Kok, S. and Monteiro, P. M. S.: Empirical methods for the estimation of Southern Ocean CO₂: support vector and random forest regression, *Biogeosciences*, 14(23), 5551–5569, doi:10.5194/bg-14-5551-2017, 2017.

Gregor, L., Kok, S. and Monteiro, P. M. S.: Interannual drivers of the seasonal cycle of CO₂ in the Southern Ocean, *Biogeosciences*, 15(8), 2361–2378, doi:10.5194/bg-15-2361-2018, 2018.

Hain, M. P., Sigman, D. M., Higgins, J. A. and Haug, G. H.: The effects of secular calcium and magnesium concentration changes on the thermodynamics of seawater acid/base chemistry: Implications for Eocene and Cretaceous ocean carbon chemistry and buffering, *Global Biogeochem. Cycles*, 29(5), 517–533, doi:10.1002/2014GB004986, 2015.

Hastie, T., Tibshirani, R. and Friedman, J. H.: *The Elements of Statistical Learning: Data mining, Inference, and Prediction*, Second Edi., Springer, 2009.

Holte, J., Talley, L. D., Gilson, J. and Roemmich, D.: An Argo mixed layer climatology and database, *Geophys. Res. Lett.*, 44(11), 5618–5626, doi:10.1002/2017GL073426, 2017.

Hoyer, S. and Hamman, J. J.: xarray: N-D labeled Arrays and Datasets in Python, *J. Open Res. Softw.*, 5, 1–6, doi:10.5334/jors.148, 2017.



- Iida, Y., Kojima, A., Takatani, Y., Nakano, T., Sugimoto, H., Midorikawa, T. and Ishii, M.: Trends in pCO₂ and sea-air CO₂ flux over the global open oceans for the last two decades, *J. Oceanogr.*, 71(6), 637–661, doi:10.1007/s10872-015-0306-4, 2015.
- Ishii, M., Inoue, H. Y., Matsueda, H. and Tanoue, E.: Close coupling between seasonal biological production and dynamics of dissolved inorganic carbon in the Indian Ocean sector and the western Pacific Ocean sector of the Antarctic Ocean, *Deep. Res. Part I Oceanogr. Res. Pap.*, 45(7), 1187–1209, doi:10.1016/S0967-0637(98)00010-7, 1998.
- Jones, S. D., Le Quéré, C., Rödenbeck, C., Manning, A. C. and Olsen, A.: A statistical gap-filling method to interpolate global monthly surface ocean carbon dioxide data, *J. Adv. Model. Earth Syst.*, 7(4), 1554–1575, doi:10.1002/2014MS000416, 2015.
- Kamenkovich, I., Cheng, W., Schmid, C. and Harrison, D. E.: Effects of eddies on an ocean observing system with profiling floats: Idealized simulations of the Argo array, *J. Geophys. Res.*, 116(6), 1–14, doi:10.1029/2010JC006910, 2011.
- Kamenkovich, I., Haza, A., Gray, A. R., Dufour, C. O. and Garraffo, Z.: Observing System Simulation Experiments for an array of autonomous biogeochemical profiling floats in the Southern Ocean, *J. Geophys. Res. Ocean.*, 1–17, doi:10.1002/2017JC012819, 2017.
- Khatiwala, S., Tanhua, T., Mikaloff Fletcher, S. E., Gerber, M., Doney, S. C., Graven, H. D., Gruber, N., McKinley, G. A., Murata, A., Rios, A. F. and Sabine, C. L.: Global ocean storage of anthropogenic carbon, *Biogeosciences*, 10(4), 2169–2191, doi:10.5194/bg-10-2169-2013, 2013.
- Landschützer, P., Gruber, N. and Bakker, D. C. E.: An updated observation-based global monthly gridded sea surface pCO₂ and air-sea CO₂ flux product from 1982 through 2015 and its monthly climatology (NCEI Accession 0160558). Version 2.2. NOAA National Centers for Environmental Information. Dataset., 2017.
- Landschützer, P., Gruber, N., Bakker, D. C. E., Stemmler, I. and Six, K. D.: Strengthening seasonal marine CO₂ variations due to increasing atmospheric CO₂, *Nat. Clim. Chang.*, 8(2), 146–150, doi:10.1038/s41558-017-0057-x, 2018.
- Landschützer, P., Gruber, N. and Bakker, D. C. E.: Decadal variations and trends of the global ocean carbon sink, *Global Biogeochem. Cycles*, 30(10), 1396–1417, doi:10.1002/2015GB005359, 2016.
- Landschützer, P., Gruber, N., Bakker, D. C. E. and Schuster, U.: Recent variability of the global ocean carbon sink, *Glob. Planet. Change*, 927–949, doi:10.1002/2014GB004853. Received, 2014.
- Landschützer, P., Gruber, N., Haumann, F. A., Rödenbeck, C., Bakker, D. C. E., Van Heuven, S. M. A. C., Hoppema, M., Metzl, N., Sweeney, C., Takahashi, T. T., Tilbrook, B. and Wanninkhof, R. H.: The reinvigoration of the Southern Ocean carbon sink, *Science* (80.-), 349(6253), 1221–1224, doi:10.1126/science.aab2620, 2015.
- Le Quéré, C., Andrew, R. M., Friedlingstein, P., Sitch, S., Hauck, J., Pongratz, J., Pickers, P., Korsbakken, J. I., Peters, G. P. and Canadell, J. G.: Global carbon budget 2018, *Earth Syst. Sci. Data*, 10, 2141–2194, doi:10.5194/essd-10-2141-2018, 2018.
- Lefèvre, N., Watson, A. J. and Watson, A. R.: A comparison of multiple regression and neural network techniques for mapping in situ pCO₂ data, *Tellus B Chem. Phys. Meteorol.*, 57(5), 375–384, doi:10.3402/tellusb.v57i5.16565, 2005.
- Lenton, A., Bopp, L. and Matear, R. J.: Strategies for high-latitude northern hemisphere CO₂ sampling now and in the future, *Deep. Res. Part II Top. Stud. Oceanogr.*, 56(8–10), 523–532, doi:10.1016/j.dsr2.2008.12.008, 2009.
- Lenton, A., Matear, R. J. and Tilbrook, B.: Design of an observational strategy for quantifying the Southern Ocean uptake of CO₂, *Global Biogeochem. Cycles*, 20(Figure 1), GB4010, doi:10.1029/2005GB002620, 2006.
- Lenton, A., Metzl, N., Takahashi, T. T., Kuchinke, M., Matear, R. J., Roy, T., Sutherland, S. C., Sweeney, C. and Tilbrook, B.: The observed evolution of oceanic pCO₂ and its drivers over the last two decades, *Global Biogeochem. Cycles*, 26(2), 1–14, doi:10.1029/2011GB004095, 2012.
- Lenton, A., Tilbrook, B., Law, R. M., Bakker, D. C. E., Doney, S. C., Gruber, N., Ishii, M., Hoppema, M., Lovenduski, N. S., Matear, R. J., McNeil, B. I., Metzl, N., Fletcher, S. E. M., Monteiro, P. M. S., Rödenbeck, C., Sweeney, C. and Takahashi, T. T.: Sea-air CO₂ fluxes in the Southern Ocean for the period 1990–2009, *Biogeosciences*, 10(6), 4037–4054, doi:10.5194/bg-10-4037-2013, 2013.
- Lueker, T. J., Dickson, A. G. and Keeling, C. D.: Ocean pCO₂ calculated from dissolved inorganic carbon, alkalinity, and equations for K₁ and K₂: Validation based on laboratory measurements of CO₂ in gas and seawater at equilibrium, *Mar. Chem.*, 70, 105–119, doi:10.1016/S0304-4203(00)00022-0, 2000.



- Majkut, J. D., Carter, B. R., Frölicher, T. L., Dufour, C. O., Rodgers, K. B. and Sarmiento, J. L.: An observing system simulation for Southern Ocean carbon dioxide uptake., *Philos. Trans. R. Soc.*, 372, 20130046--, doi:10.1098/rsta.2013.0046, 2014.
- Maritorena, S., Fanton D'andon, O. H., Mangin, A. and Siegel, D. A.: Merged satellite ocean color data products using a bio-optical model: Characteristics, benefits and issues, *Remote Sens. Environ.*, 114, 1791–1804, doi:10.1016/j.rse.2010.04.002, 2010.
- Masarie, K. A., Peters, W., Jacobson, A. R. and Tans, P. P.: ObsPack: A framework for the preparation, delivery, and attribution of atmospheric greenhouse gas measurements, *Earth Syst. Sci. Data*, 6(2), 375–384, doi:10.5194/essd-6-375-2014, 2014.
- Mazloff, M. R., Cornuelle, B. D., Gille, S. T. and Verdy, A.: Correlation Lengths for Estimating the Large-Scale Carbon and Heat Content of the Southern Ocean, *J. Geophys. Res. Ocean.*, 1–35, doi:10.1002/2017JC013408, 2018.
- McKinley, G. A., Pilcher, D. J., Fay, A. R., Lindsay, K., Long, M. C. and Lovenduski, N. S.: Timescales for detection of trends in the ocean carbon sink, *Nature*, 530(7591), 469–472, doi:10.1038/nature16958, 2016.
- McKinley, G. A., Pilcher, D. J., Fay, A. R., Lindsay, K., Long, M. C. and Lovenduski, N. S.: Timescales for detection of trends in the ocean carbon sink, *Nature*, 530(7591), 469–472, doi:10.1038/nature16958, 2016.
- Mckinney, W.: Data Structures for Statistical Computing in Python. [online] Available from:
<https://conference.scipy.org/proceedings/scipy2010/pdfs/mckinney.pdf> (Accessed 16 February 2019), 2010.
- Monteiro, P. M. S.: A Global Sea Surface Carbon Observing System: Assessment of Changing Sea Surface CO₂ and Air-Sea CO₂ Fluxes, *Proc. Ocean. Sustain. Ocean Obs. Inf. Soc.*, (1), 702–714, doi:10.5270/OceanObs09.cwp.64, 2010.
- Olsen, A., Key, R. M., van Heuven, S., Lauvset, S. K., Velo, A., Lin, X., Schirnick, C., Kozyr, A., Tanhua, T., Hoppema, M., Jutterström, S., Steinfeldt, R., Jeansson, E., Ishii, M., Pérez, F. F. and Suzuki, T.: The Global Ocean Data Analysis Project version 2 (GLODAPv2) – an internally consistent data product for the world ocean, *Earth Syst. Sci. Data*, 8(2), 297–323, doi:10.5194/essd-8-297-2016, 2016.
- Pedregosa, F., Varoquaux, G., Gramfort, A., Michel, C., Thirion, B., Grisel, O., Blondel, M., Prettenhofer, P., Weiss, R., Dubourg, V., Vanderplas, J., Passos, A. and Cournapeau, D.: Scikit-learn: Machine learning in Python, *J. Mach. Learn. Res.*, 12, 2825–2830, doi:10.1007/s13398-014-0173-7.2, 2011.
- Rio, M.-H., Mulet, S. and Picot, N.: Beyond GOCE for the ocean circulation estimate: Synergetic use of altimetry, gravimetry, and in situ data provides new insight into geostrophic and Ekman currents, *Geophys. Res. Lett.*, 41(24), 8918–8925, doi:10.1002/2014GL061773, 2014.
- Ritter, R., Landschützer, P., Gruber, N., Fay, A. R., Iida, Y., Jones, S., Nakaoka, S., Park, G.-H., Peylin, P., Rödenbeck, C., Rodgers, K. B., Shutler, J. D. and Zeng, J.: Observation-Based Trends of the Southern Ocean Carbon Sink, *Geophys. Res. Lett.*, 44(24), 12,339–12,348, doi:10.1002/2017GL074837, 2017.
- Rödenbeck, C., Bakker, D. C. E., Gruber, N., Iida, Y., Jacobson, A. R., Jones, S., Landschützer, P., Metzl, N., Nakaoka, S., Olsen, A., Park, G.-H., Peylin, P., Rodgers, K. B., Sasse, T. P., Schuster, U., Shutler, J. D., Valsala, V., Wanninkhof, R. and Zeng, J.: Data-based estimates of the ocean carbon sink variability – first results of the Surface Ocean pCO₂ Mapping intercomparison (SOCOM), *Biogeosciences*, 12(23), 7251–7278, doi:10.5194/bg-12-7251-2015, 2015.
- Rödenbeck, C., Bakker, D. C. E., Metzl, N., Olsen, A., Sabine, C., Cassar, N., Reum, F., Keeling, R. F. and Heimann, M.: Interannual sea-air CO₂ flux variability from an observation-driven ocean mixed-layer scheme, *Biogeosciences*, 11(17), 4599–4613, doi:10.5194/bg-11-4599-2014, 2014.
- Sabine, C. L., Feely, R. A., Gruber, N., Key, R. M., Lee, K., Bullister, J. L., Wanninkhof, R. H., Wong, C. S., Wallace, D. W. R., Tilbrook, B., Millero, F. J., Peng, T., Kozyr, A., Ono, T. and Ríos, A. F.: The Oceanic Sink for Anthropogenic CO₂, *Science* (80-.), 305(5682), 367–371, doi:10.1126/science.1097403, 2004.
- Sabine, C. L., Hankin, S., Koyuk, H., Bakker, D. C. E., Pfeil, B., Olsen, A., Metzl, N., Kozyr, A., Fassbender, A. J., Manke, A., Malczyk, J., Akl, J., Alin, S. R., Bellerby, R. G. J., Borges, A. V., Boutin, J., Brown, P. J., Cai, W.-J., Chavez, F. P., Chen, A., Cosca, C. E., Feely, R. A., González-Dávila, M., Goyet, C., Hardman-Mountford, N. J., Heinze, C., Hoppema, M., Hunt, C. W., Hydes, D., Ishii, M., Johannessen, T., Key, R. M., Kötzinger, A., Landschützer, P., Lauvset, S. K., Lefèvre, N., Lenton, A., Lourantou, A., Merlivat, L., Midorikawa, T., Mintrop, L., Miyazaki, C., Murata, A., Nakadate, A., Nakano, Y., Nakaoka, S., Nojiri, Y., Omar, A. M., Padin, X. A., Park, G.-H., Paterson, K.,



- Perez, F. F., Pierrot, D., Poisson, A., Rios, A. F., Salisbury, J., Santana-Casiano, J. M., Sarma, V. V. S., Schlitzer, R., Schneider, B., Schuster, U., Sieger, R., Skjelvan, I., Steinhoff, T., Suzuki, T., Takahashi, T. T., Tedesco, K., Telszewski, M., Thomas, H., Tilbrook, B., Vandemark, D., Veness, T., Watson, A. J., Weiss, R., Wong, C. S. and Yoshikawa-Inoue, H.: Surface Ocean CO₂ Atlas (SOCAT) gridded data products, *Earth Syst. Sci. Data*, 5(1), 145–153, doi:10.5194/essd-5-145-2013, 2013.
- Sasse, T. P., McNeil, B. I. and Abramowitz, G.: A novel method for diagnosing seasonal to inter-annual surface ocean carbon dynamics from bottle data using neural networks, *Biogeosciences*, 10(6), 4319–4340, doi:10.5194/bg-10-4319-2013, 2013.
- Takahashi, T., Sutherland, S. C. and Kozyr, A.: Global Ocean Surface Water Partial Pressure of CO₂ Database: Measurements Performed During 1957–2017 (Version 2017), ORNL/CDIAC-160, NDP-088(V2017). (NCEI Access. 0160492). Version 4.4. NOAA Natl. Centers Environ. Information. Dataset., doi:10.3334/CDIAC/OTG.NDP088(V2015), 2017.
- Takahashi, T. T., Sutherland, S. C., Wanninkhof, R. H., Sweeney, C., Feely, R. A., Chipman, D. W., Hales, B., Friederich, G. E., Chavez, F. P., Sabine, C. L., Watson, A. J., Bakker, D. C. E., Schuster, U., Metzl, N., Yoshikawa-Inoue, H., Ishii, M., Midorikawa, T., Nojiri, Y., Körtzinger, A., Steinhoff, T., Hoppema, M., Olafsson, J., Arnarson, T. S., Tilbrook, B., Johannessen, T., Olsen, A., Bellerby, R. G. J., Wong, C. S., Delille, B., Bates, N. R. and de Baar, H. J. W.: Climatological mean and decadal change in surface ocean pCO₂ and net sea-air CO₂ flux over the global oceans, *Deep. Res. Part II Top. Stud. Oceanogr.*, 56(8–10), 554–577, doi:10.1016/j.dsr2.2008.12.009, 2009.
- Taylor, K. E.: Summarizing multiple aspects of model performance in a single diagram, *J. Geophys. Res. Atmos.*, 106(D7), 7183–7192, doi:10.1029/2000JD900719, 2001.
- Telszewski, M., Chazottes, A., Schuster, U., Watson, A. J., Moulin, C., Bakker, D. C. E., González-Dávila, M., Johannessen, T., Körtzinger, A., Luger, H., Olsen, A., Omar, A. M., Padin, X. A., Ríos, A. F., Steinhoff, T., Santana-Casiano, M., Wallace, D. W. R. and Wanninkhof, R. H.: Estimating the monthly pCO₂ distribution in the North Atlantic using a self-organizing neural network, *Biogeosciences*, 6(8), 1405–1421, doi:10.5194/bg-6-1405-2009, 2009.
- Thomalla, S. J., Fauchereau, N., Swart, S. and Monteiro, P. M. S.: Regional scale characteristics of the seasonal cycle of chlorophyll in the Southern Ocean, *Biogeosciences*, 8(10), 2849–2866, doi:10.5194/bg-8-2849-2011, 2011.
- Verdy, A. and Mazloff, M. R.: A data assimilating model for estimating Southern Ocean biogeochemistry, *J. Geophys. Res. Ocean.*, 122(9), 6968–6988, doi:10.1002/2016JC012650, 2017.
- Wanninkhof, R. H., Bakker, D., Bates, N., Steinhoff, T. and Sutton, A.: Incorporation of Alternative Sensors in the SOCAT Database and Adjustments to Dataset Quality Control Flags, , (2009), 1–26, doi:10.3334/CDIAC/OTG.SOCAT, 2013.
- Wanninkhof, R. H., Park, G.-H., Takahashi, T. T., Sweeney, C., Feely, R. A., Nojiri, Y., Gruber, N., Doney, S. C., McKinley, G. A., Lenton, A., Le Quéré, C., Heinze, C., Schwinger, J., Graven, H. D. and Khatiwala, S.: Global ocean carbon uptake: magnitude, variability and trends, *Biogeosciences*, 10(3), 1983–2000, doi:10.5194/bg-10-1983-2013, 2013.
- Weiss, R.: Carbon dioxide in water and seawater: the solubility of a non-ideal gas, *Mar. Chem.*, 2(3), 203–215, doi:10.1016/0304-4203(74)90015-2, 1974.
- Williams, N. L., Juranek, L. W., Feely, R. A., Johnson, K. S., Sarmiento, J. L., Talley, L. D., Dickson, A. G., Gray, A. R., Wanninkhof, R. H., Russell, J. L., Riser, S. C. and Takeshita, Y.: Calculating surface ocean pCO₂ from biogeochemical Argo floats equipped with pH: An uncertainty analysis, *Global Biogeochem. Cycles*, 31(3), 591–604, doi:10.1002/2016GB005541, 2017.
- Zeng, J., Matsunaga, T., Saigusa, N., Shirai, T., Nakaoka, S. I. and Tan, Z. H.: Technical note: Evaluation of three machine learning models for surface ocean CO₂ mapping, *Ocean Sci.*, 13(2), 303–313, doi:10.5194/os-13-303-2017, 2017.
- Zeng, J., Nojiri, Y., Landschützer, P., Telszewski, M. and Nakaoka, S.: A global surface ocean fCO₂ climatology based on a feed-forward neural network, *J. Atmos. Ocean. Technol.*, 31(8), 1838–1849, doi:10.1175/JTECH-D-13-00137.1, 2014.